PNAS RESEARCH ARTICLE | APPLIED PHYSICAL SCIENCES

Emergence of disordered branching patterns in confined chiral nematic liquid crystals

Sebastián Echeverría-Alar[a,b,1], Marcel G. Clerc[a,b], and Ignacio Bordeu[a]

Edited by Tom Lubensky, University of Pennsylvania, Philadelphia, PA; received December 9, 2022; accepted March 6, 2023

Spatial branching processes are ubiquitous in nature, yet the mechanisms that drive their growth may vary significantly from one system to another. In soft matter physics, chiral nematic liquid crystals provide a controlled setting to study the emergence and growth dynamic of disordered branching patterns. Via an appropriate forcing, a cholesteric phase may nucleate in a chiral nematic liquid crystal, which self-organizes into an extended branching pattern. It is known that branching events take place when the rounded tips of cholesteric fingers swell, become unstable, and split into two new cholesteric tips. The origin of this interfacial instability and the mechanisms that drive the large-scale spatial organization of these cholesteric patterns remain unclear. In this work, we investigate experimentally the spatial and temporal organization of thermally driven branching patterns in chiral nematic liquid crystal cells. We describe the observations through a mean-field model and find that chirality is responsible for the creation of fingers, regulates their interactions, and controls the tip-splitting process. Furthermore, we show that the complex dynamics of the cholesteric pattern behaves as a probabilistic process of branching and inhibition of chiral tips that drives the large-scale topological organization. Our theoretical findings are in good agreement with the experimental observations.

liquid crystals | chirality | interface dynamics | branching process

Significance

Chirality breaks the mirror symmetry and may introduce rich new dynamics to physical systems, as observed in particle physics, condensed matter, chemical, biological, and soft matter systems. Here, we consider a liquid crystal mixed with chiral molecules to explore the role of chirality in driving the destabilization of chiral bubbles and the branching dynamics of cholesteric fingers, as a response to thermal forcing on a confined space. We show that the large-scale organization and topology of the chiral textures emerge from stochastic tip branching and inhibition. Our work provides the means to control the organization of confined cholesteric patterns and paves the way for future studies in chiral systems, such as self-organization in noncentrosymmetric magnets.

Branching processes are responsible for the formation of a vast number of ramified structures observed in geology, chemistry, biology, and physics (1). In soft matter physics, fingering instability, whereby a flat interface becomes unstable, giving rise to tip splitting, is a well-known mechanism of spatial branching (2–4). Several macroscopic models have been formulated to describe the context-dependent mechanisms of branching (1, 5–7). However, it remains a challenging task to identify the key ingredients that lead to the large-scale branching self-organized patterns in each case.

The rich phenomenology of chiral nematic liquid crystals (CNLCs) renders them an ideal system to study pattern formation and branching (8–11). CNLCs can be created by doping a nematic liquid crystal, characterized by a long-range orientational order, but not a positional one, with chiral molecules (12–14). The addition of chiral dopants can induce a spontaneous twist deformation in the nematic phase, creating a helical structure (12, 13, 15). The main feature of this phase is the characteristic length of the helix, known as cholesteric pitch p, which corresponds to the distance required for one full rotation of the nematic director vector $\vec{n}(\vec{r})$, where $\vec{r} = (x, y, z)$ is a position vector. The pitch is the mesoscopic manifestation of the molecular chirality (16), while the director vector field accounts for the local average orientation of liquid crystal molecules (17, 18). When subjected to homeotropic anchoring in a cell of thickness d, the helical phase gets frustrated, so that given a critical degree of frustration, which is measured in terms of the ratio d/p, the system transitions to an unwound (nematic) metastable state. This state is purely geometric and is sustained by the competition between the pitch, geometric effects introduced by the cell thickness, and elasticity (13, 19, 20). The twisted or winded structure can be recovered by applying a voltage, a temperature difference, or changing the thickness to the cell in the unwound state (13). In general, the reappearance of the twisted phase is in the form of a translationally invariant configuration (TIC) or in the form of cholesteric fingers of type 1 (CF1). The TIC phase is characterized by a twist along the cell thickness $\vec{n}(z)$ (*SI Appendix*, Fig. S1) and the CF1 by a director field of the general form $\vec{n}(x, y, z)$ (Fig. 1 *A*–*C* and *SI Appendix*, Fig. S1). In directional growth experiments with voltage, other types of cholesteric fingers (CF2, CF3, and CF4) have been observed (21). The recovery of the twisted structure can be described by the minimization of the Frank–Oseen free energy with an additional chiral term (*SI Appendix*) (12). This type of noncentrosymmetric interaction is also modeled in chiral magnets and in particle physics (22, 23).

Author affiliations: [a]Departamento de Física, Facultad de Ciencias Físicas y Matemáticas, Universidad de Chile, 837.0415 Santiago, Chile; and [b]Millennium Institute for Research in Optics, Facultad de Ciencias Físicas y Matemáticas, Universidad de Chile, 837.0415 Santiago, Chile

Author contributions: M.G.C. designed research; S.E.-A. and I.B. performed research; S.E.-A. and I.B. analyzed data; and S.E.-A. and I.B. wrote the paper.

The authors declare no competing interest.

This article is a PNAS Direct Submission.

[1]To whom correspondence may be addressed. Email: sebastianecheverria@ug.uchile.cl.

This article contains supporting information online at http://www.pnas.org/lookup/suppl/doi:10.1073/pnas.2221000120/-/DCSupplemental.

Published April 7, 2023.

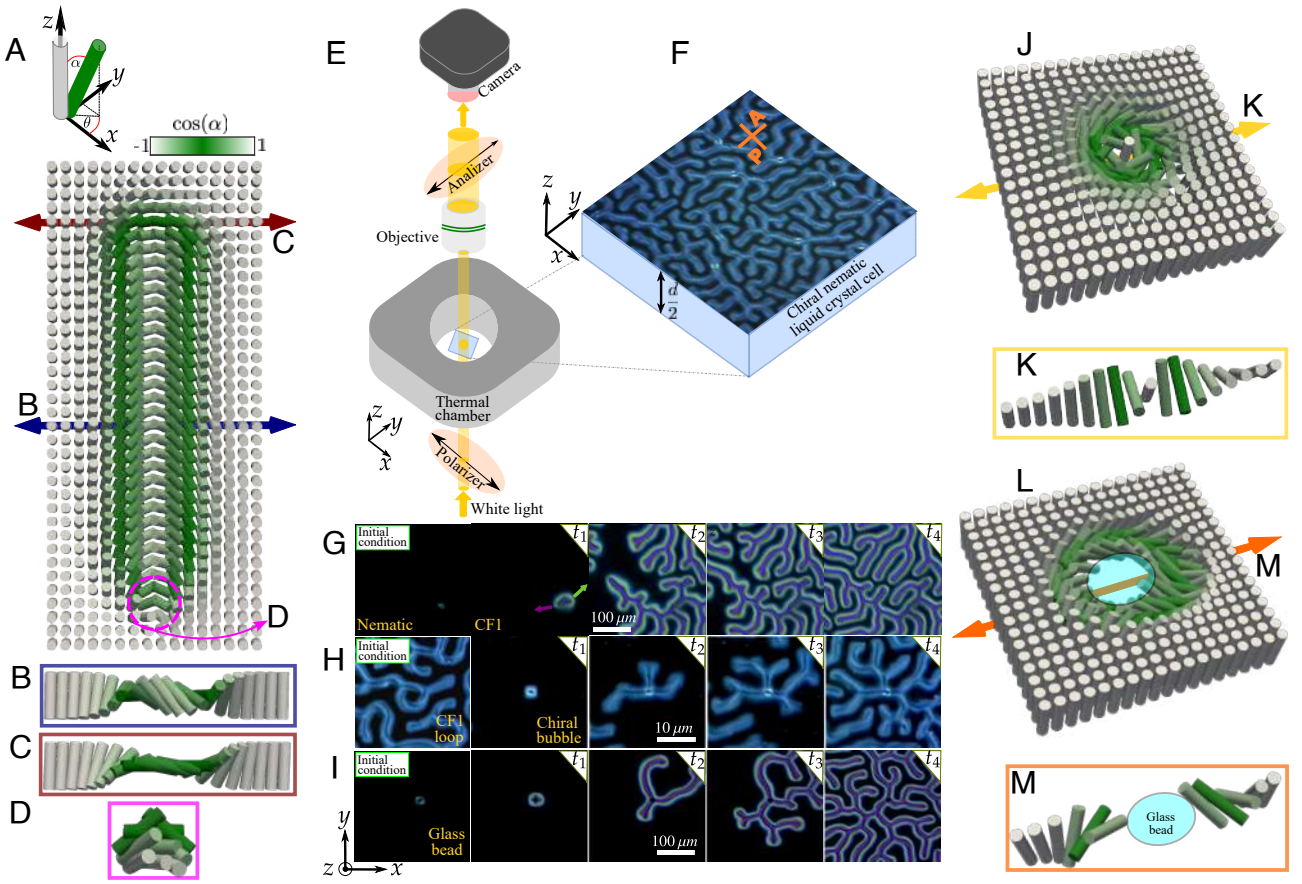

Fig. 1. Emergence of branching patterns in cholesteric liquid crystal cells. (*A–D*) and (*J–M*) display the schematic representation of the director field of the CNLC in the midplane of the cell $z = d/2$. The angles α and θ correspond to the tilt angle of $\vec{n}$ from the z-axis and the angle between the x-axis and the projection of $\vec{n}$ in the plane of the cell, respectively. (*A*) shows the CF1 director field on the plane, characterized by a good twist across its (*B*) body and (*C*) rounded tip and a localized bad twist at its (*D*) pointed tip. (*E*) Schematic representation of the experimental setup. (*F*), Steady-state cholesteric branching pattern reached after the tip-splitting dynamics. Evolution of branching patterns through the fingering instability of a cholesteric interface starting at $t_1 = 0.00$ s, which is triggered at (*G*), cholesteric fingers ($t_2 = 5.27$ s; $t_3 = 5.83$ s, $t_4 = 6.63$ s) of type I, (*H*) chiral bubbles ($t_2 = 2.62$ s; $t_3 = 3.20$ s, $t_4 = 3.41$ s), and (I), glass beads ($t_2 = 0.88$ s; $t_3 = 1.28$ s, $t_4 = 1.63$ s). The initial conditions from where the cholesteric interfaces were created are (*G*) impurities in the nematic phase, (*H*) closed loop of CF1, and (*I*) glass bead. The branching patterns (t_4) are observed at (*G*), 51.7 °C, (*H*) 51.3 °C, and (*I*) 51.7 °C. The green (purple) arrows in (*G*) illustrate the elongation of the rounded (pointed) tips of CF1. (*J*) depicts the director field of a chiral bubble on the plane, exhibiting a radial (*K*) π-twist from its center to the interface (skyrmion-like). (*L–M*) show a schematic representation of the director field build-up around a glass bead on the plane.

The winding/unwinding transition of chiral nematic liquid crystals has been widely studied from experimental and theoretical perspectives (10, 24–29). Near this transition, the distinctive CF1 appear (Fig. 1 *A–I*) (30). These elongated chiral textures nucleate from the unwound background and may elongate in arbitrary orientations from both ends. (Fig. 1*A* and *SI Appendix*, Fig. S1 for the schematic director fields in the midplane of the cell and in a cross-section along d, respectively.) The CF1 are dissipative soliton-like structures with a well-defined width that is regulated by an in-plane good twist of the nematic director (Fig. 1*B*) (25, 31). The elongation of fingers introduces the good twist in the frustrated sample. Fingers are asymmetric and exhibit two different tips, a rounded and a pointy one. The difference in morphology is associated with the handedness of the nematic director near the tips: The good twist gives rise to rounded tips (Fig. 1*C*), while the bad twist produces pointy ones (Fig. 1*D*) (25). In these frustrated CNLCs, above a critical forcing—of temperature, voltage, or confinement—fingers invade all the system through a branching dynamic. Pointy tips propagate in a straight line, nucleating rounded tips through a side-branching mechanism, and rounded tips become unstable, undergoing tip splitting as they propagate (11, 25, 32). Pointy tips, unlike rounded tips, are not generated during branching events and quickly reconnect with the cholesteric pattern or merge with impurities in the system (25). A combination of side branching and reconnection of pointy tips gives rise to closed loops of CF1. Closed loops can transform into localized twisted objects (29, 33, 34). These localized structures have been termed elementary torons, in particular, triple-twist toron-1 (35, 36). They exhibit a skyrmion-like structure in the midplane director field (36, 37) (cf. Fig. 1 *J* and *K*). Here, we refer to these elementary torons as chiral bubbles, which have also been termed spherulites (13). While more complex cholesteric textures can arise to alleviate frustration (34–36, 38), in our study, we focus only on CF1 and in the interface of chiral bubbles. Similar to glass beads, chiral bubbles can act as nucleation sites for CF1 avoiding the creation of pointy tips (29, 31), which are energetically unfavorable. Hence, the long-term dynamic of growth is governed by the continuous elongation and splitting of rounded tips, resulting in a disordered branching cover. Despite all the work conducted in frustrated CNLCs, the mechanisms that drive the tip splitting of rounded tips of CF1 and the self-organization of disordered ramified patterns have not yet been studied in detail. In this work, we study how the tip-slipping instability develops at cholesteric interfaces and which are the interaction rules that ultimately give rise to the large-scale

cholesteric branching pattern. For this, we focus on temperature-tuned chiral nematic liquid crystal experiments that allow us to control the transition toward branching and the formation of ramified patterns by heating the system. Using an adequate order parameter and its minimal model, which is derived from first principles, we demonstrate the role of chirality in the tip-splitting mechanism and the emergence of the disordered branching pattern with a velocity–curvature equation for the cholesteric interface. We show that during the growth of the chiral fingers, there is a selection principle in the morphology and speed of the rounded tip, which depends on the forcing of the system. From these analyses, we deduce a small number of crucial interactions that regulate the growth process and show that the topological features of the large-scale pattern emerge from stochastic branching and termination events.

Results

Emergence of Disordered Branching Patterns. To explore the growth of cholesteric branching patterns experimentally (Fig. 1 and *SI Appendix*, Movie S1), we consider two chiral–nematic liquid crystal cells, composed of mixtures of a commercial nematic liquid crystal E7 (Merck) and chiral molecules EOS12 (39), under thermal forcing. The cholesteric pitch p in each sample depends on the EOS12 concentration and on the temperature within the cell (14). The samples were introduced into a thermal chamber and then placed between crossed polarizers (Fig. 1*E*). In this setup, dark regions correspond to the unwound phase, while birefringent regions (shades of blue) correspond to the cholesteric phase (Fig. 1*F*). To trigger the emergence of the cholesteric phase, we initialize the experiments at room temperature (20 °C), where the CNLC is in the unwinding state, and increase the temperature at a rate of 0.35 °C min^{-1} until reaching a winding phase. Fig. 1*F* (cell #1; $T = 51.3$ °C, $p = 3.4$ μm, $d/p<58.8$; *Materials and Methods* for details) shows a steady-state of the system, which corresponds to a disordered self-organized labyrinthine pattern (40). This pattern develops mainly from the elongation and splitting of rounded tips that leads to a ramified texture, constituted locally by various connected CF1 pointing in arbitrary directions. The cholesteric fingers may be initially nucleated from impurities in the unwound phase as shown in Fig. 1*G* (cell #2; $T = 51.7$ °C, $p = 12.9$ μm, d/p=0.7) or at the cholesteric interface of a chiral bubble, which is created by cooling a closed loop of CF1 (29) (see cell #1 in Fig. 1*H*), or at the interface of glass beads, as depicted in Fig. 1*I* (cell #2), where molecular deformations are enhanced (31, 41). Under the experimental conditions considered here, the winding/unwinding transition is characterized by the emergence of CF1 (Fig. 1), instead of the TIC phase, when $d/p \approx 0.7$ and the transition temperature (T_c) is around 50 °C. In previous experiments, the TIC phase emerged subcritically in a mixture of E7 with EOS12 at 3 wt% with $d/p = 0.4$ and $T_c \approx 61.3$ °C (29). The texture selection and type of transition are governed by the elastic constants of the CNLC mixture E7-EOS12 and the confinement ratio in the cell (*SI Appendix*) (13). In consequence, in the current experimental setup, CF1 are more stable than the TIC phase.

In cells #1 and #2, the system generally avoids the creation of pointy tips by nucleating rounded tips of CF1 from chiral bubbles or glass beads instead. Therefore, the merging process of pointy tips described in the Introduction section can be neglected. We illustrate schematically the in-plane director field of the chiral bubble (Fig. 1 *J*–*K*) and around the glass bead (Fig. 1 *L*–*M*) to highlight the similarity between both interfaces and rounded tips (Fig. 1*A*). In the following, we focus our attention on the growth of fingers and their rounded tips, which can destabilize and undergo branching.

Before introducing a model to describe the rounded tip dynamic and the subsequent patterning process, we explored whether further qualitative insight into the growth process could be extracted from the spatial organization of the labyrinthine pattern (cell #2 in Fig. 2*A*). Analysis of the power spectrum of the spatial patterns (Fig. 2*B*) revealed a characteristic wavelength of $\lambda_c = 14.9\,\mu$m and powder-like ring spectrum with local order, proper of labyrinthine patterns (Fig. 2 *B*, *Inset*) (40). Furthermore, the distribution of segment lengths (defined as the distance between two branching points along the cholesteric phase) was well fitted by a gamma distribution (data in Fig. 2*C*), whose exponential tail suggests that the timing between consecutive branching events is uncorrelated (7). The typical segment length (observed as a kink for short fingers) indicates a short-term memory or maturation process between consecutive branching events of a tip. From the temporal evolution of the branching pattern, we noted that branching events could be inhibited by the neighboring pattern (green arrowheads in Fig. 2*D*), with some newly formed tips receding in favor of the growth of other, more developed tips (white arrowheads in Fig. 2*D*). These interactions lead to remodeling of the patterns, further contributing to the disordered self-organization of the patterns.

Altogether, these observations suggest that the dynamic of growth, branching, and inhibition of rounded tips controls the self-organization of the chiral labyrinthine patterns. To understand how these mechanisms arise in the context of CNLCs, in the following, we introduce a Ginzburg–Landau-type model that allows us to relate the interaction mechanisms to the chiral nature of the liquid crystal.

The Chiral–Anisotropic Ginzburg–Landau (CAGL) Model. Close to the winding/unwinding transition and in the long-pitch limit of the chiral nematic liquid crystal, the following model can be derived (*SI Appendix* for details)

$$\partial_t A = \mu A + \beta |A|^2 A - |A|^4 A + \partial_\eta \partial_{\bar\eta} A + \delta \partial_\eta \partial_\eta \bar{A} + i\chi \left(A \partial_{\bar\eta} A + \bar{A} \partial_\eta A \right), \qquad [1]$$

where $A(x, y, t) = \alpha e^{i\theta}$ is the complex order parameter close to the transition (26), $\partial_\eta = \partial_x + i\partial_y$ is the Wirtinger derivative, and $\bar{A}$ is the complex conjugate of A. Here, μ is the bifurcation parameter describing the winding/unwinding transition, while the parameter $\beta = \beta(K_{12}, K_{32}, d/p)$ controls the type of bifurcation, which is subcritical ($\beta > 0$) for the experiments considered here (29). The elastic coupling, characterized by the parameter $\delta = (K_{12} - 1)/2(K_{12} + 1)$ (42), considers both isotropic and anisotropic effects. The last term breaks the mirror symmetry in the plane of the cell and is controlled by the parameter $\chi = \chi(K_{12}, K_{32}, d/p)$. $K_{12} = K_1/K_2$, $K_{32} = K_3/K_2$, where the parameters $\{K_1, K_2, K_3\}$ are the elastic constants of the CNLC (12). The model (**1**) is variational, i.e., $\partial_t A = -\delta \mathcal{F}[A, \bar{A}]/\delta \bar{A}$, where

$$\mathcal{F} = \int\int dxdy \Big[-\mu |A|^2 - \beta \frac{|A|^4}{2} + \frac{|A|^6}{3} + |\nabla A|^2 + 2\delta Re\left\{ (\partial_\eta \bar{A})^2 \right\} - i\chi |A|^2 (\partial_{\bar\eta} A - \partial_\eta \bar{A}) \Big], \qquad [2]$$

is the free energy of the system, which is minimized during the dynamics of Eq. **1**.

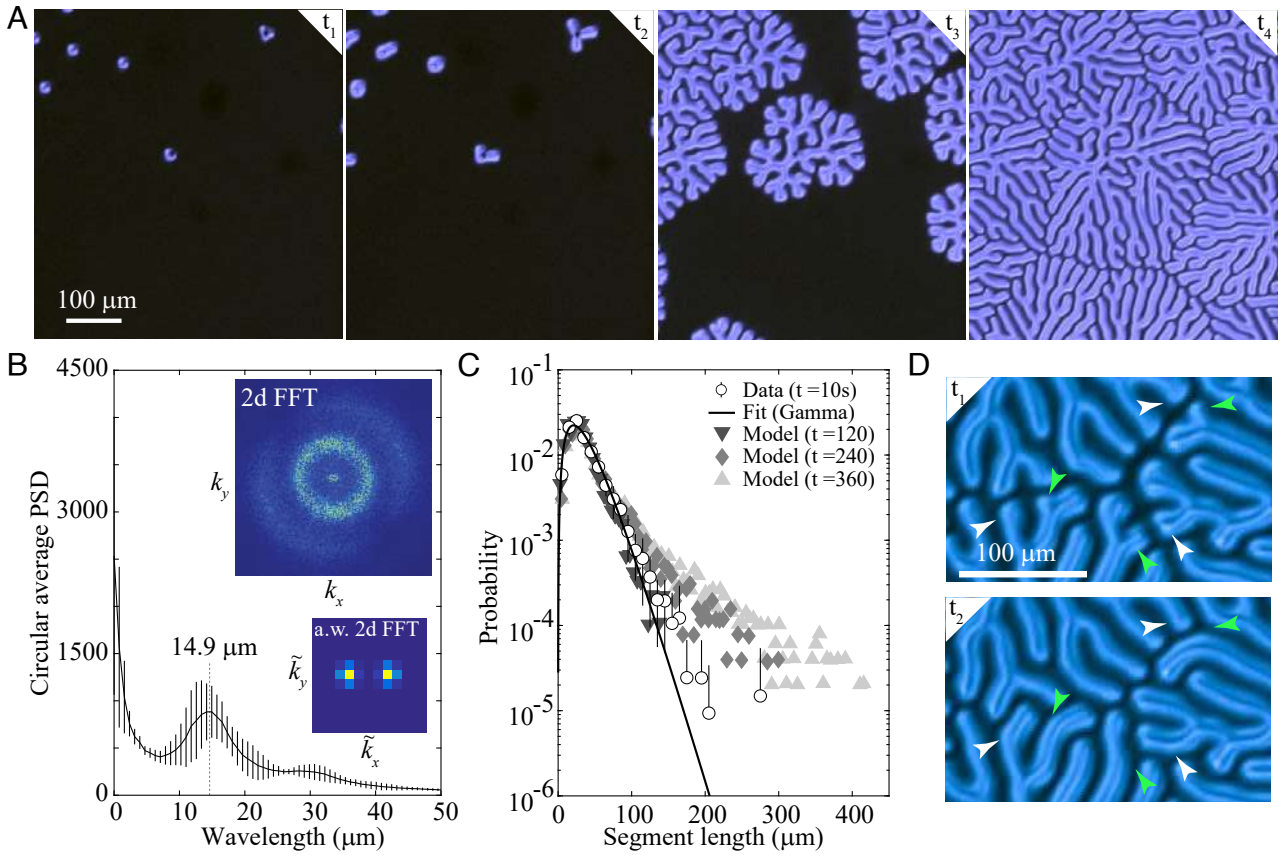

Fig. 2. Tip-branching drives the formation of a cholesteric labyrinthine pattern. (*A*), Time lapse of the destabilization of multiple cholesteric interfaces around glass beads (cell #2 with $d/p = 0.7$) and formation of an extended labyrinthine pattern, at times $t_1 = 3.3$ s, $t_2 = 7.8$ s, $t_3 = 12.2$ s, and $t_4 = 16.7$ s. (*B*), Circular average of the 2D power spectrum (*Inset Top*) of the extended pattern in panel (*A*) at t_4, showing a characteristic wavelength of the cholesteric pattern of $\lambda_C = 14.9$ microns and (*Inset Bottom*) local Fourier transform characterizing the local order in the pattern. (*C*), segment length distribution of the experimental labyrinthine patterns (markers, with errors obtained from 7 independent realizations) and a gamma distribution fit (solid line, for scale and shape parameters), together with the distribution obtained from numerical integration of Eq. **1** at three different times, rescaled by the ratio of the experimental and model wavelengths $\lambda_C/\lambda_{CAGL} \approx 2.3$. (*D*), Two time points ($t_1 < t_2$) of the experiment, showing remodeling of the patterns, where short fingers are inhibited (green arrowheads) allowing other fingers to continue elongating (white arrowheads).

The CAGL Eq. **1** exhibits the same equilibria observed in CNLC experiments: a homeotropic phase $A_o = 0$ (region I in Fig. 3*A*); a translationally invariant configuration (TIC) phase A_T (region II in Fig. 3*A*); a modulated TIC (starting in region II and crossing the green curve into region V or VI in Fig. 3*A*), chiral finger states (region IV in Fig. 3*A*); chiral bubbles (region III in Fig. 3*A*); and cholesteric labyrinths (starting in region IV and crossing the blue curve into region V in Fig. 3*A*) (13, 29). Additionally, the model (1) has a region of bistability of states A_o and A_T ($\mu_{lb} \leq \mu \leq \mu_{ub}$) that contains a Maxwell point μ_{MP}, where both states are energetically equivalent $\mathcal{F}[A_o] = \mathcal{F}[A_T]$ (43). The model also exhibits fingers and tip splitting (*Right* panels of Fig. 3*A*), where fingers nucleate from the homeotropic phase or from a chiral bubble and invade the system through elongation (region IV of Fig. 3*A*) or branching of their rounded tips (region V of Fig. 3*A*). Note that the fingers emerge at $\mu < \mu_{MP}$ (region V in Fig. 3*A*), where the state A_o is more stable than A_T. In brief, the appearance of a finger with a given width is not explained by a modulational instability, as in the case of the modulated TIC phase (13).

To understand the emergence of the chiral fingers from an energy minimization perspective, we first study the properties of an infinite finger in the CAGL Eq. **1**. In the top panel of Fig. 3*B*, the polarized field $\psi(x, y) \equiv \mathrm{Re(A)Im(A)}$ of the infinite finger solution is shown, together with the horizontal profile of its modulus R and phase gradient $\partial_x\phi$, where we use the polar representation $A(x, y) = Re^{i\phi}$. The profiles show bell-shaped soliton structures, which are characterized by their heights ($\bar{R}$ and $\bar{\Phi}$) and widths (w and w_ϕ), and can be approximated by $R \approx \bar{R}\mathrm{sech}(x/w)$ and $\partial_x\phi \approx -\bar{\Phi}\mathrm{sech}(x/w_\phi)$, respectively. Introducing these ansatz into the free energy (2), we obtain (*SI Appendix*)

$$\mathcal{F}_{finger} = F_o w + \frac{2(1+\delta)}{3w}\bar{R}^2 + (1+\delta)\bar{R}^2\bar{\Phi}^2 I_5(w, w_\phi) + 2\chi\bar{R}^3 I_6(w, w_\phi, \bar{\Phi}) - 2\chi\bar{R}^3\bar{\Phi} I_7(w, w_\phi, \bar{\Phi}), \quad [3]$$

where $F_o = -2\mu\bar{R}^2 - 2\beta\bar{R}^4/3 + 16\bar{R}^6/45$, and I_5, I_6, I_7 are integrals, which depend on the coupling between R, ϕ, and $\partial_x\phi$.

The finger solution is supported by the homogenous state ($\mathcal{F}[A_o] = 0$) if $\mathcal{F}_{finger} < 0$. The energy term F_o is bounded from below $F_o \geq (1.68\sqrt{|\mu|} - 0.67)\bar{R}^4$, which is positive for $\mu < \mu_{MP}$. Hence, the only energetic contribution that stabilizes the finger solution is the chirality, proportional to χ in Eq. **3**, while all the other terms in Eq. **3** act as a nucleation barrier. To find the optimal finger width, we minimize the free energy Eq. **3** with respect to w in the limit $w/L \ll 1$, $w_\phi/L \ll 1$, where L is the length of the finger in the y-direction. As a result of the dependence on the integrals in Eq. **3**, we can only find

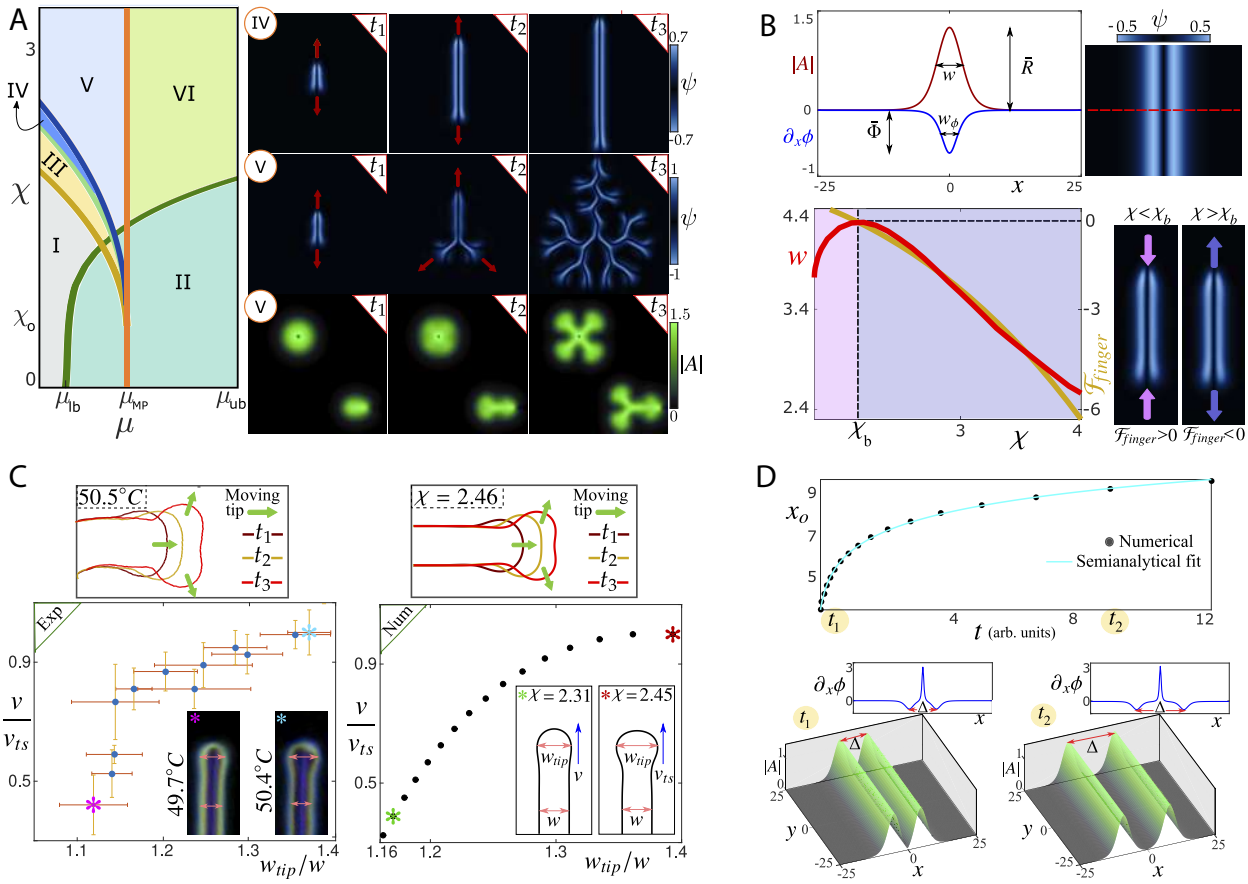

Fig. 3. Local ingredients for the appearance of cholesteric labyrinths. (*A*), Phase diagram of Eq. **1** with $\delta = 0.05$ and $\beta = 1$. $\mu_{lb} = -1/4$ and $\mu_{ub} = 0$ are the boundaries of the bistability region between A_o (I) and A_T (II). $\mu_{MP} = -3/16$ is the Maxwell point. χ_o is the critical chirality, where chiral bubbles appear. The dark yellow line marks the saddle-node transition of chiral bubbles. The light green curve delimits the emergence of chiral fingers. The blue line represents the tip-splitting instability. Region III is the stable zone of chiral bubbles. In region IV, fingers enlarge from their tips. Rounded tips of chiral fingers are unstable in region V. Regions V and VI exhibit modulated TIC. *Right* panels show temporal snapshots for three different initial conditions with $\mu = -0.4$, in the regions IV ($\chi = 2.31$) and V ($\chi = 2.70$). (*B*) shows (top) the profiles of the modulus $|A|$ and the gradient of the phase (ϕ) in the x-direction $\partial_x\phi$ of an infinite chiral finger, with $\chi = 2.4$ and $\mu = -0.4$, and (*Bottom*) shows the variation of the finger width w with respect to χ (red line) in the one-dimensional case, with $\chi_b = 2.3$ when $\mu = -0.4$; the yellow line shows the change in free energy $\mathcal{F}_{finger}$. The insets show the polarized field of chiral fingers with $\chi = 2.2 < \chi_b$ and $\chi = 2.4 > \chi_b$, exhibiting shrinking and elongation, respectively. (*C*), Different morphologies of chiral fingers were observed experimentally in cell #2 with $d/p \approx 0.68$ (*Left* panel) and numerically (*Right* panel) with $\mu = -0.4$. In the experimental case, the graph shows the speed of the rounded tip against the shape factor w_{tip}/w for different temperatures (the variations of the pitch with temperature in *SI Appendix*, Fig. S2). w_{tip} is the biggest diameter within the rounded tip of the chiral finger, and w is the width of the finger far from the rounded tip. The insets show the morphologies associated with 49.7 °C (pink asterisk) and 50.4 °C (light blue asterisk). Dots are the average of five fingers moving inside a cell of CNLC. The vertical and horizontal bars are the SD of the speed and the shape factor, respectively. In model Eq. **1**, the different morphologies are obtained by varying the χ parameter. The insets display the finger shapes in the case of $\chi = 2.31$ (green asterisk) and $\chi = 2.45$ (orange asterisk). The tip-splitting regime is shown for both cases (50.5 °C and $\chi = 2.46$). Three snapshots ($t_1 = 0.0$ s, $t_2 = 0.25$ s, and $t_3 = 0.4$ s) of the chiral fingers interface are shown, demonstrating the advance, flattening, and modulation of the rounded tips. All speeds are normalized to the average speed previous to tip-splitting v_{ts}. In the experiment, $v_{ts} = 27.4$ μm s^{-1}. (*D*), (*Top*) Evolution of the distance $x_o(t)$ in the repulsion between two infinite fingers for $\mu = -0.4$ and $\chi = 2.5$. Black dots were obtained from direct simulations, and the solid line corresponds to the integration of Eq. **5**. The *Bottom* panels display two instants, t_1 and t_2, of the repulsive dynamics.

a relationship between the optimal parameters of the finger solution; $w^3 \approx 3\pi^3\chi w_\phi^3\bar{R}^3\bar{\Phi}/4F_o$ (*SI Appendix*). Therefore, the nontrivial phase structure plays a fundamental role in defining the width, and F_o must be positive to observe stable finger solutions, i.e., the most stable homogenous state needs to be A_o. Note that a similar energy dependence is obtained in bistable reaction–diffusion systems (6).

The bottom panel of Fig. 3*B* shows the variation of the one-dimensional finger width w as a function of the chirality χ (red curve), which has a maximum at $\chi = \chi_b$. When $\chi > \chi_b$, the free energy $\mathcal{F}_{finger}$ (Eq. **3**) becomes negative (yellow line in the *Bottom* panel of Fig. 3*B*) and the system favors the propagation of fingers by elongation of the two tips (*Bottom Right* panels of Fig. 3*B*). Conversely, when $\chi < \chi_b$, the chiral finger shrinks and eventually disappears due to the merging of both tips.

When chiral fingers emerge, they propagate and cover the whole system. In the experiment of CNLCs, the temperature specifies the pitch and finger width and fixes the propagation speed of CF1, v. We note that the chiral finger growth has a selection mechanism similar to that observed in dendritic growth (44, 45), where the propagation speed is controlled by the curvature of the tip. By increasing the temperature, fingers propagate faster, and the tip swells, as shown in Fig. 3*C*.

CF1 may be characterized morphologically by the shape factor w_{tip}/w, where w_{tip} is the diameter of the rounded tip and w is the finger width (cell #2 in the left panel of Fig. 3*C*). At the critical speed v_{ts} and corresponding critical shape factor, propagating tips become unstable, swelling and undergoing tip splitting. This branching process may be interpreted as a more efficient dissipation mechanism to develop chirality than simple tip

propagation. The tip-splitting dynamics is characterized by the inflation, flattening, and interfacial modulation of the rounded tip (see the snapshots $t_1 - t_3$ in the *Left* panel of Fig. 3*C*). The *Right* panel of Fig. 3*C* shows the change in morphology in numerical integrations of Eq. **1** for different values of the chiral parameter χ. Remarkably, the relation between speed and shape obtained through numerical simulations closely resembles the experimental observations. The critical value of the shape factor at which tip splitting takes place is close to its experimental value $w_{tip}/w \approx 1.4$, and in both cases, tips suffer the same curvature and morphological changes during branching.

One way to understand the emergence of tip splitting is to analyze it from the perspective of local interface dynamics (5, 6). Recently, a local zero-dimensional interface equation was derived from Eq. **1** near the critical point $\{\mu_{MP}, \chi_o\}$ for chiral bubbles (29). There, it was shown that a balance between metastability, a linear curvature term due to chirality, and a squared curvature contribution defined the size of chiral bubbles. Here, to describe the tip-splitting instability, one needs to account for the spatial modulation along the interface and the proper stabilization mechanism at small wavelengths. We model the interface of the rounded tip as the interface of half of the chiral bubble in model Eq. **1**. The tip splitting is analogous then to a fourth mode instability of the interface of a full cholesteric bubble as shown in the *Bottom Right* panel of Fig. 3*A*. Therefore, to extract the curvature dynamics of the interface, we perform a nonlinear stability analysis around the interface of the chiral bubble solution, $A_{cb} = R_o e^{i\phi}$ in Eq. **1** and obtain the speed-curvature or Gibbs–Thomson (46) relation

$$v_N = -|\mu_1|A + B\chi_1\tilde{\kappa} + C\tilde{\kappa}^3 + D\partial_{SS}\tilde{\kappa}, \qquad [4]$$

where A, B, C, and D are constants (*SI Appendix*). A similar version of Eq. **4** has been heuristically proposed to explore the local behavior of interface dynamics (5), derived in the study of growth laws of droplets (47) and bistable reaction–diffusion systems (6) and also used in the framework of bacterial growth (48). The constants A, B, and D are always positive above the dark yellow line in the phase diagram of Fig. 3*A*. For large wavelength perturbations, Eq. **4** has a modulational instability due to a Mullins–Sekerka type of term (linear in curvature $\tilde{\kappa}$), which is tuned by the chirality, i.e., growth is enhanced in curved regions of the interface. At short wavelengths, the instability is saturated by the last term in Eq. **4**, which plays the role of line tension. The cubic term in Eq. **4** is responsible for the tip splitting, where the constant C is defined by a nontrivial balance between chirality, diffusion, and energy differences between states, and it must be positive to ensure that the curvature dynamics is variational (*SI Appendix*). The relation between curvature and splitting explains why a tip must swell before branching, a dynamic that also explains the maturation (or refractory period) feature observed earlier in the segment length distribution (Fig. 2*C*).

Another key ingredient for the formation of the cholesteric branching patterns is the repulsion between the chiral fingers (25). To study the origin of the CF1 repulsion in our model, Eq. **1**, we consider two infinite cholesteric fingers. The *Bottom* panels of Fig. 3*D* show two different instants of the interaction between two cholesteric fingers, where a nontrivial structure in the gradient of the phase is observed between the two fingers. As it turns out, this structure is responsible for the repulsion between fingers. Following this idea and the symmetry of the modulus R and the phase gradient $\partial_x\phi$, we model the repulsion between fingers as the interaction between a single finger, at a position $x_o(t)$ from the origin, and half of the phase structure near $x = 0$, that is, $R(t) = R(x - x_o(t))$ and $\partial_x\phi(t) = \partial_x\phi(x - x_o(t)) + \theta_b(x)$, where $A(t) = R(t)e^{i\phi(t)}$ and θ_b represents the phase structure near $x = 0$. Numerical observations show that the tail of θ_b decays like e^{-bx}/x for a positive constant b. Based on the variational form of model Eq. **1**, the dynamic of the position x_o is given by (*SI Appendix*)

$$\partial_t x_o = \mathcal{N}(\mu, \chi)\frac{e^{-bx_o}}{x_o}. \qquad [5]$$

The prefactor $\mathcal{N}(\mu, \chi)$ is positive in the range of parameters where chiral fingers are observed (region IV and V of Fig. 3*A*). Thus, the interaction between fingers is repulsive in order to minimize the energy of the system. By integrating the repulsive relationship, we get the semianalytical curve $x_o(t)$ shown in the *Top* panel of Fig. 3*D*.

Organization of the Large-Scale Chiral Branching Pattern. In the previous section, we described how the local destabilization of the nematic phase leads to the propagation of a chiral (or cholesteric) phase, which organizes into a ramified pattern that expands through the propagation of chiral tips. The chirality drives the growth and splitting of tips as well as the repulsion between fingers. From the propagation of the branching pattern (experiment Fig. 2*A* and model Fig. 4*A*), we note that actively elongating and branching tips localize entirely at the periphery of the growing pattern, while tips submerged within the labyrinthine structure arrest their growth due to steric interactions with the surrounding pattern. The interactions that give rise to the branching cholesteric pattern can be reduced then to tip propagation and branching, repulsion (that results in alignment of neighboring segments), and tip inhibition. Moreover, the characteristic width of CF1 combined with the energy minimization dynamics leads to a spatial pattern structure with a well-defined wavelength, with a short-scale order but large-scale disorder (Fig. 2*B*).

To study how the large-scale disorder emerges from the local interaction rules, we first focused on the model (1), which allowed us to study the topological properties of large-scale patterns without the influence of additional structures (Fig. 4*A*). From these patterns, we were able to extract the branching trees (Fig. 4*B*), produced by reducing the pattern to a network of vertices and edges, where each edge corresponds to a chiral segment that connects vertices representing branching points. Here, we were concerned solely with the topology of the network, which is completely characterized by the levels (or generations) of branching. The subtrees of the network, defined as sets of branches with a last common ancestor node at level 2, showed a high heterogeneity of sizes (number of segments) and persistence (number of generations beyond level 2); see colored subtrees in Fig. 4 *A* and *B* indicating a rather random organization of the topology of the pattern as seen, for example, in biological tissues (7, 49, 50). A heterogeneous organization of the branching tree may arise from a stochastic process of branching and inhibition of propagating chiral tips, which was also supported by the exponential decay of segment lengths (Fig. 2*C*). To test this hypothesis, we computed the probability that tips at a given level arrest their growth (Fig. 4*C*). As time passes, tips that are not constrained may continue branching, lowering the termination probability. We then simulated a zero-dimensional birth–death process, where particles either branched or became inhibited with probabilities depending on their generations and given by Fig. 4*C* (*Methods* for details). To compare the results of the

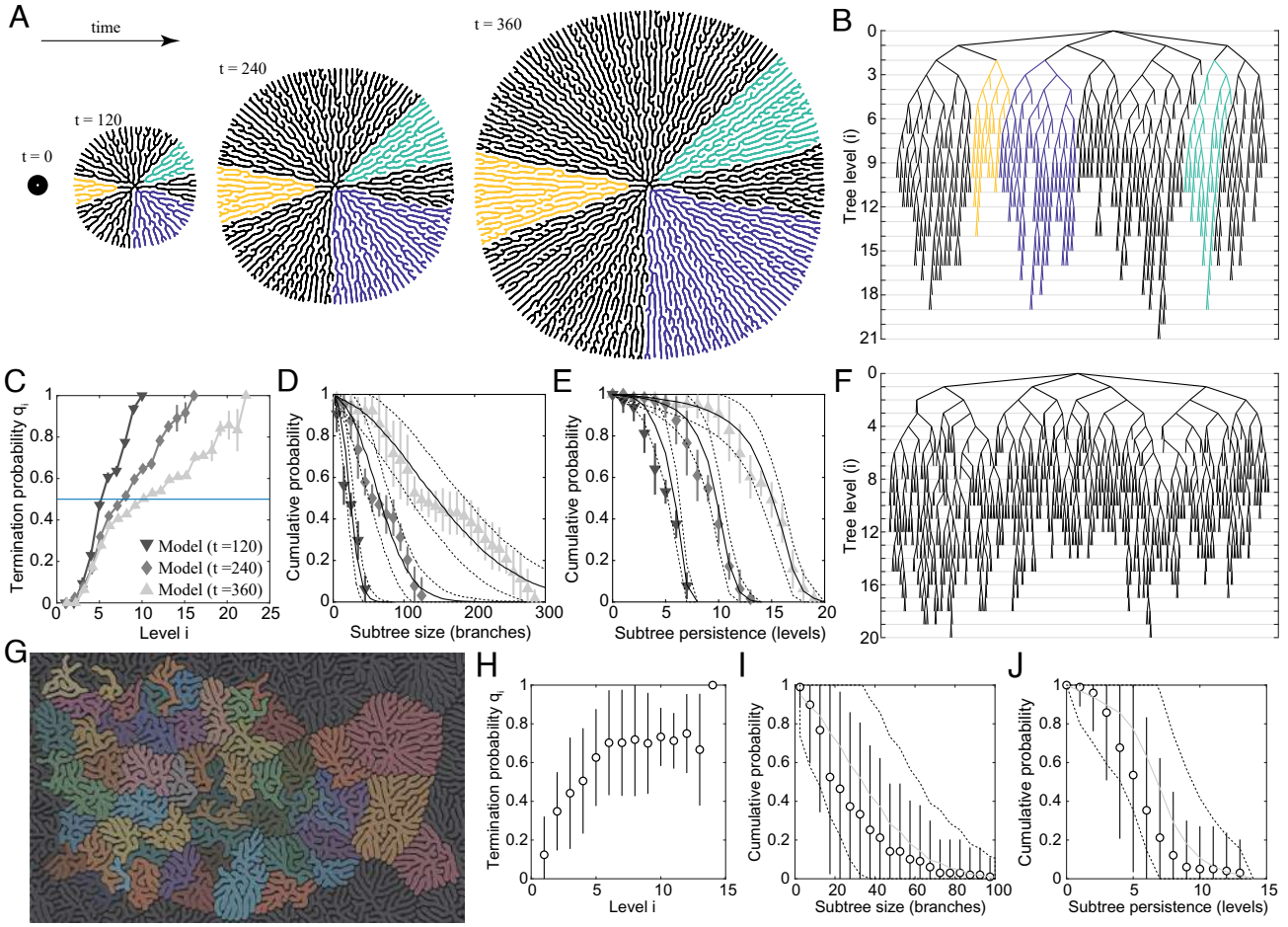

Fig. 4. The large-scale organization emerges from probabilistic tip branching and inhibition events. (*A*), Numerical integration of the Eq. **1** showing the destabilization of a chiral bubble-like initial condition ($t = 0$) into a branched pattern ($t = 240$ and $t = 360$, measured in arbitrary units). Subtrees of the branching structure, defined as those trees that have a last common ancestor at branching level 2, are colored at different times to emphasize the variability in the tree growth dynamics. (*B*), Branching tree representation of the pattern at time $t = 360$, shown in (*A*). (*C*) The probability that a tip terminates at a given level in the tree at different time point obtained from $n = 8$ large-scale simulations of the model (1). (*D* and *E*) show the cumulative probability of (*D*) subtree sizes and (*E*) subtree persistence obtained from large-scale simulations of the model (mean and SD from $n = 8$ realizations) and birth–death process when supplied with the termination probabilities at each time point in (*C*), with mean (line) and SD (shaded) from $n = 10^3$ realizations. (*F*), Branching tree resulting from the birth–death process using as input the termination probabilities at $t = 360$ shown in (*C*). (*G*), Representative stationary state from experiments; disconnected branching patterns are shown in different colors, and black-shaded patterns were not considered in the analysis as they cross the boundaries of the observation window. (*H*), Average termination probability obtained from 39 disconnected branching patterns from 7 experimental realizations. (*I* and *J*) show the cumulative probability of (*D*) tree sizes and (*E*) tree persistence (full trees were used due to their small size) obtained from experiments (mean and SD) and birth–death process when using the termination probabilities in (*G*) as input.

model (1) and the stochastic birth–death process, we looked at the distribution of subtree sizes and persistence, from which we found excellent agreement (Fig. 4 *C* and *D*). These results show that even though the system has well-defined interaction rules, their large-scale organization emerges from random events of branching and termination that are regulated locally, at the single tip level (see the typical branching tree from the birth–death process in Fig. 4*F*).

To verify that these observations also apply to the experimental branching patterns, we looked at 7 realizations of the experiments, where multiple distinct patterns nucleated from the glass beads in the sample (Figs. 1*E* and 4*G*). The final patterns had a range of sizes and interacted as they developed, in some cases inhibiting the growth of neighboring tips. By focusing on trees with more than one branching event, we reconstructed the termination probability (Fig. 4*H*) and used it as input in the stochastic birth–death process. These resulted, again, in good agreement between experiments and the stochastic process (Fig. 4 *I* and *J*, where full trees were analyzed due to their small size), strongly supported the conclusion that the large-scale topology of the chiral branching patterns is regulated locally by statistical rules of branching and termination, resulting in the disordered patterns observed.

In summary, we have investigated experimentally and theoretically the spatial and temporal organization of thermally induced branching patterns in chiral nematic liquid crystal cells. By using the Ginzburg–Landau-type description of CNLCs, we established the role of chirality in the formation of disordered branching patterns. Here, the (de)stabilization of chiral fingers arises from an energy minimization process, which also leads to tip splitting and causes repulsive interactions between fingers. We extracted a minimal set of local rules that regulate the pattern growth—tip elongation, branching, repulsion, and inhibition—and showed that the large-scale organization of the branching pattern described a stochastic birth–death process, where branching and termination events are probabilistic in nature. The large-scale organization of the chiral phase emerges then from local interactions at the single tip level, which minimizes energy efficiently through branching.

Our analyzes show that even though the liquid crystal structure is inherently 3D, the dynamics of growth of the branching phase follows simple local rules that take place on the 2D midplane, resulting in branching and inhibition of tips. Therefore, neglecting the three-dimensional liquid crystal structure is a good approximation for studying the formation of disordered branching patterns resulting from CF1 destabilization. An interesting future direction of research is to explore other finger structures, such as CF2, CF3, and CF4 (21) and investigate their space-filling dynamics. Additionally, in the broader context, it will be interesting to explore possible branching processes of stripe phases in chiral magnets (51).

Materials and Methods

Materials and Experimental Setup. We consider a chiral liquid crystal composed of a mixture of a commercial multicomponent nematic liquid crystal E7 (pure components: 4-cyano-4′-n-pentyl-1,1′- biphenyl (5CB-51\%); 4-cyano-4′-n-heptyl-1,1′- biphenyl (7CB-25\%); 4-cyano-4′-n-octyloxy-1,1′- biphenyl (8OCB-16\%); 4-cyano-4″-n-pentyl- 1,1′,1″ -terphenyl (5CT-8\%)) from Merck with chiral molecules EOS-12 (4-(5-dodecylthio-1,3,4-oxadiazole-2-yl)phenyl 4′-(1″-methyl heptyl-oxy)benzoate) at 25 wt% and 7 wt%. The cholesteric pitch p associated with each chiral–nematic mixture is measured with the Grandjean–Cano technique at the temperatures of observation, by using a planoconvex cylindrical lens of radius 10.3 mm (Thorlabs) as thickness modulation. Two cell preparations were implemented. In the first one, a chiral liquid crystal droplet (with EOS-12 at 25 wt%) is deposited over a soda-lime glass sheet using a microcapillary tube and covered with another sheet of the same characteristics (2.5 cm×2.5 cm area and 4 mm thickness). This type of glass induces a homeotropic anchoring on the liquid crystal sample. The squeezed disk-shaped droplet reaches an equilibrium diameter of approximately 1 cm. The cell obtained with this method is cell #1 with $d = 200\ \mu$m. The cell thickness was obtained with a Mitutoyo digital micrometer with an accuracy of 1 μm. We note that to increase the resolution of the images of chiral bubbles, we used a 50x objective with a small working distance (Leica, HC PL APO 50x/0,90). Then, in our experimental setup, it was unavoidable to squeeze cell #1 with the objective, thus pushing the cell thickness to an effective value $d < 200\ \mu$m. For this reason, this cell was used exclusively for observational purposes (Fig. 1 *F* and *H*). The second method is by filling chiral nematic liquid crystals (with EOS-12 at 7 wt%), by capillary action at 70 °C, into a fabricated cell (SG025T090uT180 manufactured by Instec) of thickness $d = 9\ \mu$m, which is chemically treated to give homeotropic boundary conditions, and its thickness is fixed by glass beads. This cell, #2, was used in the experimental measurements discussed in the text (Figs. 2, 3*C*, and 4 *G–J*) and in the observations shown in Fig. 1 *G* and *I*. The prepared cells are introduced into a LinkamT95-PE hot stage and placed between crossed polarizers in a Leica DM2700P microscope with 5x, 10x, and 50x objectives. A CMOS camera records the branching dynamics.

Numerical Integration of the Chiral–Anisotropic Ginzburg–Landau Equation. To solve model Eq. **1**, we write the equation in terms of its real part u and imaginary part v ($A = u + iv$). Then, we discretize the space by using a finite difference scheme with a spatial step of $\Delta x = 0.25$ and a three-point stencil using nonflux boundary conditions. The coupled equations for u and v are numerically integrated in time with the Runge–Kutta 4 time integrator with temporal step $\Delta t = 0.01$. The finger solutions shown in Fig. 3 were created by perturbing the zero solution with a rectangular perturbation of width $2w$ and amplitude $(u, v) = (1.5, 0)$ in region IV of the phase diagram in Fig. 3*A*. Depending on the proximity of the tips to the boundaries (with nonflux boundary conditions), we can annihilate tips and create fingers only with rounded tips (Fig. 3*C*) and without tips (Fig. 3 *B* and *D*). The chiral bubble solutions are created following the experiment. We start with a finger in region IV and sweep the parameter χ or μ to access the branching region V of the phase diagram in Fig. 3*A*. The pointy tip of a finger can merge with a side branch and create a CF1 loop solution (29). Then we change the parameters into region III and the CF1 loop solution collapses into the chiral bubble solution. This localized solution is used as the initial condition in Figs. 3*A* and 4*A* (in the branching region V). All the numerical results related to Fig. 3 are obtained in square grids of size 200*x*200. In the case of Fig. 4*A*, we used a square grid of size 1000*x*1000.

Shape Factor w_{tip}/w and Speed of CF1. To characterize the morphology of the chiral fingers, we introduced in the text the dimensionless shape factor w_{tip}/w. The width w of the fingers is calculated as the finite width at half-maximum of the transversal profiles of the fingers from the binarized images in the experiment and from the numerical solutions of Eq. **1**. We determine the diameter of the tip w_{tip} as the diameter of the biggest circle that fits the rounded tips of CF1. Once the biggest circle is fitted in the rounded tip of a CF1, we track the position of the tip and measure its speed v. In the experimental case, mixture of E7 and EOS-12 at 7 wt% within cell #2 with $d/p \approx 0.68$, we averaged the width, tip diameter, and speed of five fingers, which are seen under crossed polarizers at different temperatures. Finally, the criteria to determine the tip-splitting speed v_{ts} is when the far-most point of the rounded tip interface has zero curvature (flat front).

Numerical Simulation of the Stochastic Birth–Death Process. The topology and statistics of a branching tree depend on the growth dynamic and how tips interact with the surrounding structures. In particular, the exponential decay of segment lengths in the chiral branching tree (Fig. 2*C*) suggests that the branching and termination events are uncorrelated, thus following a Poisson-like process, albeit with a short refractory period. With this in mind, we questioned whether the large-scale topology of the branching tree could be fully characterized by its branching (and terminating) probabilities. For this, we formulated a simple birth–death model: a zero-dimensional branching process, where tip branching and terminations follow a stochastic rule. In this birth–death model, which has also been used to describe ramified biological tissues (49), tips are allowed to branch and terminate with probabilities estimated from the data. These probabilities are obtained from the termination probabilities q_i (Fig. 4 *C* and *H*) and depend exclusively on the generation in the branching tree. We note that if the birth–death model was not able to recapitulate the branching topology of the tree, then it would indicate that correlations and spatial considerations would indeed be essential to the resulting large-scale chiral pattern. Numerically, the birth–death model was implemented as a discrete-time process, where, at every iteration, all active (tip) particles were allowed to either branch (with probability $p_{\text{branch}} = 1 - q_i$) or become inactive (inhibited) with probability $p_{\text{inhib}} = q_i$, depending on the generation i at which the particles are. For this, we initialized the system with a number $N \geq 1$ of particles to match the initial state observed either in the model (1) or the experiments. For each realization, we kept track of the history of all particles in order to reconstruct the branching trees (Fig. 4*F*).

Data, Materials, and Software Availability. The raw data used for this study are available in Zenodo repository (DOI: https://doi.org/10.5281/zenodo.7753119). All other study data are included in the article and/or *SI Appendix*.

ACKNOWLEDGMENTS. We acknowledge P.I. Hidalgo and J. Vergara for the synthetization of the cholesteric liquid crystal. M.G.C. thanks for the financial support of ANID-Millenium Science Initiative Program–ICN17_012 (MIRO) and FONDECYT project 1210353. I.B. acknowledges the financial support from FONDECYT project 11230941 and the Universidad de Chile-VID project UI-015/22. We also thank Gregorio González-Cortés for fruitful discussions. Sources of funding: -ANID by Beca Doctorado Nacional 2020- 21201376. -ANID-Millenium Science Initiative Program–ICN17_012 (MIRO) -FONDECYT project 1210353.

1. V. Fleury, J. F. Gouyet, M. Leonetti, *Branching in Nature: Dynamics and Morphogenesis of Branching Structures, from Cell to River Networks* (Springer Science, Business Media, 2001), vol. 14.
2. P. G. Saffman, G. I. Taylor, The penetration of a fluid into a porous medium or Hele-Shaw cell containing a more viscous liquid. *Proc. R. Soc. London. Ser. A. Math. Phys. Sci.* **245**, 312–329 (1958).
3. A. Buka, J. Kertész, T. Vicsek, Transitions of viscous fingering patterns in nematic liquid crystals. *Nature* **323**, 424–425 (1986).
4. K. J. Lee, W. McCormick, Q. Ouyang, H. L. Swinney, Pattern formation by interacting chemical fronts. *Science* **261**, 192–194 (1993).
5. R. C. Brower, D. A. Kessler, J. Koplik, H. Levine, Geometrical approach to moving-interface dynamics. *Phys. Rev. Lett.* **51**, 1111 (1983).
6. R. E. Goldstein, D. J. Muraki, D. M. Petrich, Interface proliferation and the growth of labyrinths in a reaction-diffusion system. *Phys. Rev. E* **53**, 3933 (1996).
7. E. Hannezo *et al*., A unifying theory of branching morphogenesis. *Cell* **171**, 242–255 (2017).
8. A. Stieb, Structure of elongated and spherulitic domains in long pitch cholesterics with homeotropic boundary alignment. *J. de Phys.* **41**, 961–969 (1980).
9. P. Oswald, J. Bechhoefer, A. Libchaber, Instabilities of a moving nematic-isotropic interface. *Phys. Rev. Lett.* **58**, 2318 (1987).
10. P. Ribiere, S. Pirkl, P. Oswald, Electric-field-induced phase transitions in frustrated cholesteric liquid crystals of negative dielectric anisotropy. *Phys. Rev. A* **44**, 8198 (1991).
11. T. Nagaya, Y. Hikita, H. Orihara, Y. Ishibashi, Experimental study of the growth of the cholesteric finger pattern. *J. Phys. Soc. Japan* **65**, 2707–2712 (1996).
12. P. G. de Gennes, J. Prost, *The Physics of Liquid Crystals* (Clarendon Press, Oxford, UK, ed. 2, 1993).
13. P. Oswald, P. Pieranski, *Nematic and Cholesteric Liquid Crystals* (CRC Press, London, 2005).
14. I. Dierking, *Textures of Liquid Crystals* (John Wiley & Sons, 2003).
15. A. B. Harris, R. D. Kamien, T. C. Lubensky, Molecular chirality and chiral parameters. *Rev. Mod. Phys.* **71**, 1745 (1999).
16. S. Pieraccini, S. Masiero, A. Ferrarini, G. P. Spada, Chirality transfer across length-scales in nematic liquid crystals: Fundamentals and applications. *Chem. Soc. Rev.* **40**, 258–271 (2011).
17. H. De Vries, Rotatory power and other optical properties of certain liquid crystals. *Acta Crystallogr.* **4**, 219–226 (1951).
18. R. Cano, Interprétation des discontinuités de grandjean. *Bull. de Minéral.* **91**, 20–27 (1968).
19. W. E. Haas, J. E. Adams, Electrically variable diffraction in spherulitic liquid crystals. *Appl. Phys. Lett.* **25**, 263–264 (1974).
20. N. Nawa, K. Nakamura, Observation of forming process of bubble domain texture in liquid crystals. *Japan. J. Appl. Phys.* **17**, 219 (1978).
21. J. Baudry, S. Pirkl, P. Oswald, Topological properties of singular fingers in frustrated cholesteric liquid crystals. *Phys. Rev. E* **57**, 3038 (1998).
22. R. Takagi *et al*., Spin-wave spectroscopy of the Dzyaloshinskii-Moriya interaction in room-temperature chiral magnets hosting skyrmions. *Phys. Rev. B* **95**, 220406 (2017).
23. T. H. R. Skyrme, A unified field theory of mesons and baryons. *Nucl. Phys.* **31**, 556–569 (1962).
24. F. Lequeux, P. Oswald, J. Bechhoefer, Influence of anisotropic elasticity on pattern formation in a cholesteric liquid crystal contained between two plates. *Phys. Rev. A* **40**, 3974 (1989).
25. P. Ribiere, P. Oswald, Nucleation and growth of cholesteric fingers under electric field. *J. de Phys.* **51**, 1703–1720 (1990).
26. T. Frisch, L. Gil, J. M. Gilli, Two-dimensional Landau-de Gennes dynamical model for the unwinding transition of a cholesteric liquid crystal. *Phys. Rev. E* **48**, R4199 (1993).
27. L. Gil, Numerical resolution of the cholesteric unwinding transition problem. *J. de Phys.* **II** (5), 1819–1833 (1995).
28. S. Thiberge, Ph.D. thesis (Université de Nice–Sophia Antipolis) (1999).
29. M. G. Clerc, G. González-Cortés, S. Echeverría-Alar, Localized dissipative vortices in chiral nematic liquid crystal cells. *Phys. Rev. Res.* **4**, L022021 (2022).
30. P. Oswald, J. Baudry, S. Pirkl, Static and dynamic properties of cholesteric fingers in electric field. *Phys. Rep.* **337**, 67 (2000).
31. I. I. Smalyukh *et al*., Electric-field-induced nematic-cholesteric transition and three-dimensional director structures in homeotropic cells. *Phys. Rev. E* **72**, 061707 (2005).
32. P. Oswald, J. Baudry, T. Rondepierre, Growth below and above the spinodal limit: The cholesteric-nematic front. *Phys. Rev. E* **70**, 041702 (2004).
33. J. Baudry, S. Pirkl, P. Oswald, Looped finger transformation in frustrated cholesteric liquid crystals. *Phys. Rev. E* **59**, 5562 (1999).
34. J. S. B. Tai, P. J. Ackerman II, Smalyukh,, Topological transformations of Hopf solitons in chiral ferromagnets and liquid crystals. *Proc. Natl. Acad. Sci. U.S.A.* **115**, 921–926 (2018).
35. P. J. Ackerman II, Smalyukh,, Diversity of knot solitons in liquid crystals manifested by linking of preimages in Torons and Hopfions. *Phys. Rev. X* **7**, 011006 (2017).
36. I. I. Smalyukh, Y. Lansac, N. A. Clark, R. P. Trivedi, Three-dimensional structure and multistable optical switching of triple-twisted particle-like excitations in anisotropic fluids. *Nat. Mater.* **9**, 139–145 (2010).
37. S. Muhlbauer *et al*., Skyrmion lattice in a chiral magnet. *Science* **323**, 915–919 (2009).
38. I. I. Smalyukh, Knots and other new topological effects in liquid crystals and colloids. *Rep. Progr. Phys.* **83**, 106601 (2020).
39. M. L. Parra, P. I. Hidalgo, E. Y. Elgueta, Synthesis and mesomorphic properties of oxadiazole esters derived from (r)-2-octanol,(s)-2-n-octyloxypropanol and (2 s, 3 s)-2-chloro-3-methylpentanol. *Liq. Cryst.* **35**, 823–832 (2008).
40. S. Echeverría-Alar, M. Clerc, Labyrinthine patterns transitions. *Phys. Rev. Res.* **2**, 042036 (2020).
41. V. Zambra, M. G. Clerc, R. Barboza, U. Bortolozzo, S. Residori, Umbilical defect dynamics in an inhomogeneous nematic liquid crystal layer. *Phys. Rev. E* **101**, 062704 (2020).
42. T. Frisch, S. Rica, P. Coullet, J. M. Gilli, Spiral waves in liquid crystal. *Phys. Rev. Lett.* **72**, 1471 (1994).
43. R. E. Goldstein, G. H. Gunaratne, L. Gil, P. Coullet, Hydrodynamic and interfacial patterns with broken space-time symmetry. *Phys. Rev. A* **43**, 6700 (1991).
44. J. S. Langer, Instabilities and pattern formation in crystal growth. *Rev. Mod. Phys.* **52**, 1 (1980).
45. E. Ben-Jacob, P. Garik, The formation of patterns in non-equilibrium growth. *Nature* **343**, 523–530 (1990).
46. L. M. Pismen, *Patterns and Interfaces in Dissipative Dynamics* (Springer Science & Business Media, 2006).
47. D. Gomila, P. Colet, G. L. Oppo, M. San Miguel, Stable droplets and growth laws close to the modulational instability of a domain wall. *Phys. Rev. Lett.* **87**, 194101. (2001).
48. L. Xiong *et al*., Flower-like patterns in multi-species bacterial colonies. *Elife* **9**, e48885 (2020).
49. C. L. Scheele *et al*., Identity and dynamics of mammary stem cells during branching morphogenesis. *Nature* **542**, 313–317 (2017).
50. F. J. Roos *et al*., Human branching cholangiocyte organoids recapitulate functional bile duct formation. *Cell Stem Cell* **29**, 776–794 (2022).
51. X. Wang, X. Hu, H. Wu, Stripe skyrmions and skyrmion crystals. *Commun. Phys.* **4**, 142 (2021).

Supporting Information for

Emergence of disordered branching patterns in confined chiral nematic liquid crystals

Sebastián Echeverría-Alar, Marcel G. Clerc and Ignacio Bordeu

Sebastián Echeverría-Alar.
E-mail: sebastianecheverria@ug.uchile.cl

This PDF file includes:

Supporting text
Figs. S1 to S3
Legend for Movie S1
SI References

Other supporting materials for this manuscript include the following:

Movie S1

Supporting Information Text

Derivation of the chiral-anisotropic Ginzburg-Landau (CAGL) model. The CAGL model can be derived from first principles, based on the dissipative dynamics of the director field $\vec{n}(\vec{r},t)$, where $\vec{r}$ and t indicate spatial and temporal dependence, respectively. This procedure gives a unique dependence of the parameters μ, β, δ, and χ with the elastic constants and the confinement ratio d/p of chiral nematic liquid crystal (CNLC) cells. We are interested in the experimental situation where a nematic phase $\vec{n} \equiv \vec{n}_o$, induced by the homeotropic anchoring of a cell with thickness d, is invaded by a cholesteric phase $\vec{n} \equiv \vec{n}(\vec{r})$ in the form of cholesteric fingers of type I (CF1) when energy is injected in the system. In our case, an increase in temperature is the injection of energy, but it could also be an electric field (1).

The starting point is a continuum theory for the chiral nematic liquid crystal. We follow a simple approach and suppose that in a weakly distorted regime, the local properties of the material are the ones of a uniaxial liquid crystal (2). This supposition allows us to write the Frank-Oseen free energy

$$F_{ed} = \int \left[\frac{K_1}{2}(\nabla \cdot \vec{n})^2 + \frac{K_2}{2}(\vec{n} \cdot \nabla \wedge \vec{n} + 2\pi/p)^2 + \frac{K_3}{2}(\vec{n} \wedge \nabla \wedge \vec{n})^2 \right] d\vec{r}, \qquad [1]$$

where K_1, K_2, and K_3 are the splay, twist, and bend elastic constants, respectively. The volumetric free energy F_{ed} is valid in the limit of strong anchoring where surface terms can be neglected. The cholesteric pitch p needs to be big, compared to a molecular scale, so the supposition of uniaxiality remains valid (3). When energy is injected into the system, the molecules will dissipate it following a minimization process that can be accounted by the evolution of the director $\vec{n}(\vec{r},t)$, while maintaining its unitary norm (4)

$$\gamma \frac{d\vec{n}}{dt} = -\frac{\delta F_{ed}}{\delta \vec{n}} + \vec{n}\left(\vec{n} \cdot \frac{\delta F_{ed}}{\delta \vec{n}}\right), \qquad [2]$$

where γ is a rotational viscosity constant. Then, introducing the free energy Eq. (1) into Eq. (2), one obtains (5)

$$\begin{aligned} \gamma \frac{d\vec{n}}{dt} &= K_3[\nabla^2\vec{n} - \vec{n}(\vec{n} \cdot \nabla^2\vec{n})] + (K_3 - K_1)[\vec{n}(\vec{n} \cdot \nabla)(\nabla \cdot \vec{n}) - \nabla(\nabla \cdot \vec{n})] \\ &+ (K_2 - K_3)[2(\vec{n} \cdot \nabla \wedge \vec{n})\{\vec{n}(\vec{n} \cdot \nabla \wedge \vec{n}) - \nabla \wedge \vec{n}\} + \vec{n} \wedge \nabla(\vec{n} \cdot \nabla \wedge \vec{n})] + \frac{4\pi K_2}{p}[-\nabla \wedge \vec{n} + \vec{n}(\vec{n} \cdot \nabla \wedge \vec{n})], \end{aligned} \qquad (3)$$

with the homeotropic boundary conditions, $\vec{n}(x,y,z=0) = \vec{n}(x,y,z=d) = \hat{z}$. Note that the last term accounts for the torque induced by chiral effects.

We perform a linear stability analysis of the homeotropic nematic phase $\vec{n}_o = (0,0,1)$ against small perturbations to find the critical confinement ratio d/p, at which the winding/unwinding transition is developed. Then, we replace the perturbative ansatz $\vec{n} = (n_1, n_2, \sqrt{1-n_1^2-n_2^2})$ into Eq. (3) and retain only linear terms in n_1 and n_2, which leads to the coupled equations

$$\gamma \frac{\partial n_1}{\partial t} = K_3 \partial_{zz} n_1 + \frac{4\pi K_2}{p} \partial_z n_2, \qquad [4]$$

$$\gamma \frac{\partial n_2}{\partial t} = K_3 \partial_{zz} n_2 - \frac{4\pi K_2}{p} \partial_z n_1. \qquad [5]$$

Note that the third component of the perturbation was restrained to higher order corrections in n_1 and n_2 due to the norm conservation $|\vec{n}| = 1$. The next step is to find the condition at which the first unstable winding mode grows, that is, we consider an ansatz of the form $n_1 = \alpha_o \cos(fz)\sin(\pi z/d)e^{\sigma t}$ and $n_2 = \alpha_o \sin(fz)\sin(\pi z/d)e^{\sigma t}$. These components satisfy the homeotropic boundary conditions at $z=0$ and $z=d$ (see Fig. S1a) and correspond to a helicoidal rotation at rate f within the cell. The linear growth rate is σ and a_o is a constant. The rotation of the director components in the z-axis is motivated by the translationally invariant configuration (TIC) phase (see Fig. S1b). We incorporate the ansatz $n_1(z,t)$ and $n_2(z,t)$ in Eqs. (4) and (5), and set the marginal stability condition $\sigma = 0$ to obtain the critical rate $f_c = 2\pi/pK_{32}$ and the critical confinement $d_c/p = K_{32}/2$, where $K_{32} = K_3/K_2$. Indeed the helical structure of the chiral nematic liquid crystal will be recovered when a critical confinement ratio is surpassed (1, 6).

Close to the critical confinement ratio, winding/unwinding transition, we perform a weakly nonlinear analysis to find the slow spatiotemporal dynamics of the director $\vec{n}$ near this critical point and to saturate the instability revealed by the linear analysis. In the nonlinear regime, we need to take into account the spatial variations of n_1 and n_2 in the plane x-y. Only with this consideration, for example, we are able to observe CF1 (see Fig. S1c). A simple way to consider the spatial dependence near the winding/unwinding transition is by introducing the following director field (7, 8)

$$\begin{pmatrix} n_1 \\ n_2 \\ n_3 \end{pmatrix} \approx \begin{pmatrix} \cos(f_c z + \theta)\sin\left(\alpha \sin\left(\frac{\pi z}{d_c}\right)\right) \\ \sin(f_c z + \theta)\sin\left(\alpha \sin\left(\frac{\pi z}{d_c}\right)\right) \\ \cos\left(\alpha \sin\left(\frac{\pi z}{d_c}\right)\right) \end{pmatrix}, \qquad [6]$$

where $\alpha=\alpha(x,y,t)$ and $\theta=\theta(x,y,t)$ correspond to the angle tilt of $\vec{n}$ from the z-axis, and the angle between the x-axis and the projection of $\vec{n}$ in the plane of the cell, respectively (Fig. S1). Both α and θ vary slowly in space and time. Note that Eq. (6) is the representation on the surface of the unit sphere S2 of the TIC texture plus a bidimensional modulation modeled by θ (1, 7, 9). In the limit $\alpha \ll 1$, we may introduce the complex small order parameter $A(x,y,t)\equiv \alpha e^{i\theta}\equiv Re(A)+iIm(A)\equiv u+iv$ to describe the behavior of CNLCs close to the winding/unwinding transition (7). Then, we write Eq. (6) in terms of u and v

$$\begin{pmatrix} n_1 \\ n_2 \\ n_3 \end{pmatrix} \approx \begin{pmatrix} u\cos\left(\frac{\pi z}{d_c}\right)\sin\left(\frac{\pi z}{d_c}\right) - v\sin^2\left(\frac{\pi z}{d_c}\right) + W_1^{[3]} + W_1^{[5]} + \cdots \\ v\cos\left(\frac{\pi z}{d_c}\right)\sin\left(\frac{\pi z}{d_c}\right) + u\sin^2\left(\frac{\pi z}{d_c}\right) + W_2^{[3]} + W_2^{[5]} + \cdots \\ 1-\frac{n_1^2}{2}-\frac{n_2^2}{2}-\frac{n_1^4}{8}-\frac{n_2^4}{8}-\frac{n_1^2 n_2^2}{4}+\cdots \end{pmatrix}, \quad [7]$$

where $W_1^{[3]}$, $W_1^{[5]}$, $W_2^{[3]}$, and $W_2^{[5]}$ are higher nonlinear corrections of order cubic and quintic in A, respectively. Now, we substitute the previous ansatz into Eq. (3) and at order $\vec{W}^{[3]}=(W_1^{[3]},W_2^{[3]})$, we obtain

$$\gamma\partial_t ucs-\gamma\partial_t vs^2 = -2\frac{\pi^2}{d^2}K_3 us_2-2\frac{\pi^2}{d^2}K_3 vc_2+K_3\partial_{zz}W_1^{[3]}+K_3\frac{\pi^2}{d^2}(usc-vs^2)(u^2+v^2)+K_3(\partial_{xx}+\partial_{yy})ucs-K_3(\partial_{xx}+\partial_{yy})vs^2+(K_3-K_1)\frac{\pi^2}{d^2}\left\{-(ucsc_2-vs^2c_2)(u^2+v^2)+\frac{d^2}{\pi^2}(-\partial_{xx}ucs+\partial_{xx}vs^2)+\frac{d}{\pi}[s_2u\partial_x u+s_2v\partial_x v+\frac{s_2^2}{2}u\partial_y u+\frac{c_2s_2}{2}u\partial_y v-s^2s_2v\partial_y u-s^2c_2v\partial_y v+\frac{s_2c_2}{2}u\partial_x u-\frac{s_2^2}{2}u\partial_x v-s^2c_2v\partial_x u+s^2s_2v\partial_x v]\right\}+(K_1-K_2)\left\{\partial_{xy}us^2+\partial_{xy}vcs\right\}+(K_2-K_3)\left\{\partial_{yy}ucs-\partial_{yy}vs^2-2\frac{\pi^2}{d^2}\left[\frac{u^3}{2}s_2s^2c_2-\frac{u^2v}{2}s_2^2s^2+\frac{u^2v}{4}s_2^2c_2-\frac{uv^2}{4}s_2^3-u^2vs^4c_2+uv^2s^4s_2-\frac{uv^2}{2}s^2s_2c_2+\frac{v^3}{2}s^2s_2^2+u^3s_2s^4+u^2vs_2^2s^2+\frac{uv^2}{4}s_2^3+u^2vs^4c_2+uv^2s^2s_2c_2+\frac{v^3}{4}c_2s_2^2+\frac{u^3}{2}s_2^3+u^2vs_2^2c_2+\frac{uv^2}{2}s_2c_2^2-u^2vs^2s_2^2-2uv^2s^2s_2c_2-v^3s^2c_2^2-u^3s^2s_2c_2-u^2vs^2c_2^2+u^2vs^2s_2^2+uv^2s^2s_2c_2-\frac{u^2v}{2}s_2^2c_2-\frac{uv^2}{2}s_2c_2^2+\frac{uv^2}{2}s_2^3+\frac{v^3}{2}s_2^2c_2\right]-\frac{2\pi}{d}\left[-s_2s^2u\partial_x u-\frac{s_2^2}{2}u\partial_x v+\frac{s_2^2}{2}u\partial_y u-s_2s^2u\partial_y v-c_2s^2v\partial_x u-\frac{c_2s_2}{2}v\partial_x v+\frac{c_2s_2}{2}v\partial_y u-c_2s^2v\partial_y v\right]+\frac{\pi}{d}\left[\frac{s_2^2}{2}u\partial_y u-s_2s^2u\partial_y v+\frac{c_2s_2}{2}v\partial_y u-c_2s^2v\partial_y v+s^2s_2u\partial_x u+s^2c_2u\partial_x v+\frac{s_2^2}{2}v\partial_x u+\frac{s_2c_2}{2}v\partial_x v-2s^2c_2u\partial_y u+2s^2s_2u\partial_y v-s_2c_2v\partial_y u+s_2^2v\partial_y v+\frac{s_2^2}{2}u\partial_y u+\frac{c_2s_2}{2}u\partial_y v-s^2s_2v\partial_y u-c_2s^2v\partial_y v-c_2s^2u\partial_y u-\frac{c_2s_2}{2}u\partial_y v+s_2s^2v\partial_y u+\frac{s_2^2}{2}v\partial_y v\right]\right\}+\frac{4\pi^2K_2}{dp}(us_2+vc_2)+\frac{4\pi K_2}{p}\partial_z W_2^{[3]}+\frac{4\pi K_2}{p}\left\{[u\partial_x u-v\partial_x v+u\partial_y v+v\partial_y u]s^3c+[v\partial_y v+u\partial_x v]c^2s^2+[u\partial_y u-v\partial_x u]s^4\right\}+\frac{4\pi^2K_2}{dp}\left\{-\frac{s_2^3}{4}u^3+\frac{s_2^2s^2}{2}u^2v+\frac{s_2c_2s^2}{2}uv^2-c_2s^4v^3+\frac{s_2c_2s^2}{2}u^3-\frac{s_2^3}{4}uv^2-c_2s^4u^2v+\frac{s_2^2s^2}{2}v^3\right\},$$

$$\gamma\partial_t us^2+\gamma\partial_t vcs = 2\frac{\pi^2}{d^2}K_3 uc_2-2\frac{\pi^2}{d^2}K_3 vs_2+K_3\partial_{zz}W_2^{[3]}+K_3\frac{\pi^2}{d^2}(us^2+vcs)(u^2+v^2)+K_3(\partial_{xx}+\partial_{yy})us^2+K_3(\partial_{xx}+\partial_{yy})vcs+(K_3-K_1)\frac{\pi^2}{d^2}\left\{-(us^2c_2+vcsc_2)(u^2+v^2)-\frac{d^2}{\pi^2}(\partial_{yy}us^2+\partial_{yy}vcs)+\frac{d}{\pi}[s_2u\partial_y u+v\partial_y v+s^2c_2u\partial_x u-s^2s_2u\partial_x v+\frac{s_2c_2}{2}v\partial_x u-\frac{s_2^2}{2}v\partial_x v+s^2s_2u\partial_y u+s^2c_2u\partial_y v+\frac{s_2^2}{2}v\partial_y u+\frac{c_2s_2}{2}v\partial_y v]\right\}+(K_1-K_2)\left\{\partial_{xy}ucs-\partial_{xy}vs^2\right\}+(K_2-K_3)\left\{\partial_{xx}us^2+\partial_{xx}vcs+\frac{2\pi^2}{d^2}\left[\frac{u^3}{4}s_2^2c_2-\frac{u^2v}{4}s_2^3-u^2vs_2c_2s^2+uv^2s_2^2s^2+uv^2c_2s^4-v^3s^4s_2+\frac{u^3}{2}s_2^2s^2+\frac{u^2v}{4}s_2^3-u^2vs_2s^4-\frac{uv^2}{2}s_2^2s^2+\frac{u^2v}{2}s_2c_2s^2+\frac{uv^2}{4}s_2^2c_2-uv^2c_2s^4-\frac{v^3}{2}c_2s^2s_2-u^3s^2c_2^2+2u^2vs^2c_2s_2-uv^2s^2s_2^2-\frac{u^2v}{2}s_2c_2^2+uv^2c_2s_2^2-\frac{v^3}{2}s_2^3+\frac{u^3}{2}s_2^2c_2+\frac{u^2v}{2}s_2c_2^2-\frac{u^2v}{2}s_2^3-\frac{uv^2}{2}s_2^2c_2-u^2vs^2s_2c_2-uv^2s^2c_2^2+uv^2s^2s_2^2+v^3s^2s_2c_2\right]-\frac{2\pi}{d}\left[c_2s^2u\partial_x u+\frac{c_2s_2}{2}u\partial_x v-\frac{c_2s_2}{2}u\partial_y u+c_2s^2u\partial_y v-s_2s^2v\partial_x u-\frac{s_2^2}{2}v\partial_x v+\frac{s_2^2}{2}v\partial_y u-s_2s^2v\partial_y v\right]+\frac{\pi}{d}\left[-\frac{s_2^2}{2}u\partial_x u+s_2s^2u\partial_x v-\frac{c_2s_2}{2}v\partial_x u+s^2c_2v\partial_x v-s_2^2u\partial_x u-\frac{c_2s_2}{2}u\partial_x v+2s_2s^2v\partial_x u+2c_2s^2v\partial_x v+\frac{s_2c_2}{2}u\partial_y u-\frac{s_2^2}{2}u\partial_y v-s^2c_2v\partial_y u+s^2s_2v\partial_y v+c_2s^2u\partial_x u+\frac{c_2s_2}{2}u\partial_x v-s_2s^2v\partial_x u-\frac{s_2^2}{2}v\partial_x v+s^2c_2u\partial_x u-s^2s_2u\partial_x v+\frac{s_2c_2}{2}v\partial_x u-\frac{s_2^2}{2}v\partial_x v\right]\right\}+\frac{4\pi^2K_2}{dp}(-uc_2+vs_2)-\frac{4\pi K_2}{p}\partial_z W_1^{[3]}-\frac{4\pi K_2}{p}\left\{[u\partial_y u-v\partial_y v-u\partial_x v-v\partial_x u]s^3c+[v\partial_y u+u\partial_x u]c^2s^2+[v\partial_x v-u\partial_y v]s^4\right\}+\frac{4\pi^2K_2}{dp}\left\{-\frac{s_2^2s^2}{2}u^3+c_2s^4uv^2-\frac{s_2^2s^2}{2}uv^2+c_2s^4u^3-\frac{s_2^3}{4}u^2v+\frac{s_2c_2s^2}{2}v^3+\frac{c_2s_2s^2}{2}u^2v-\frac{s_2^3}{4}v^3\right\}.$$

We have used the simplified notation $d = d_c$, $c = \cos(\pi z/d)$, $s = \sin(\pi z/d)$, $c_2 = \cos(2\pi z/d)$, and $s_2 = \sin(2\pi z/d)$. The above equations are an inhomogeneous linear problem on $\vec{W}^{[3]}$ of the form $\mathcal{L}\vec{W}^{[3]} = \vec{b}$, where

$$\mathcal{L} = \begin{pmatrix} K_3\partial_{zz} & \frac{4\pi K_2}{p}\partial_z \\ -\frac{4\pi K_2}{p}\partial_z & K_3\partial_{zz} \end{pmatrix}, \quad [8]$$

and $\vec{b} = (b_1, b_2)$ is the collection of all the other terms. To solve the inhomogeneous problem $\mathcal{L}\vec{W}^{[3]} = \vec{b}$, we must introduce an inner product to apply a solvability condition, i.e., the linear inhomogeneous equation will have a solution if and only if $\vec{b}$ is orthogonal to the $Ker\{\mathcal{L}^\dagger\}$. Let us consider the canonical inner product $\langle\vec{g}|\vec{h}\rangle = \int_0^d \vec{g}\cdot\vec{h}dz$, in order to be able to project the dynamics $(\vec{b})$ in the elements of $Ker\{\mathcal{L}^\dagger\}$. Note that $\mathcal{L} = \mathcal{L}^\dagger$ is self-adjoint. The elements of the kernel are $Ker\{\mathcal{L}^\dagger\} = \{\mathcal{H}_1, \mathcal{H}_2\} = \{(\cos(\pi z/d)\sin(\pi z/d), \sin^2(\pi z/d)), (\sin^2(\pi z/d), -\cos(\pi z/d)\sin(\pi z/d))\}$. The next step is to apply the solvability conditions, that is, $\langle\mathcal{H}_1|\vec{b}\rangle = 0$ and $\langle\mathcal{H}_2|\vec{b}\rangle = 0$. After straightforward calculations and combining the resulting two equations using $A = u + iv$, we get

$$\begin{aligned}\frac{\gamma}{2K_2}\partial_t A = \frac{\pi^2}{d^2}(2\mathcal{C} - K_{32})A - \frac{\pi^2}{4d^2}(3 + K_{12} - 6K_{32} + 6\mathcal{C})|A|^2A + \frac{K_{12}+1}{4}\nabla^2 A + \\ \frac{1-K_{12}}{8}\partial_\eta\partial_\eta\bar{A} + \frac{\pi}{8d}(3 - 4K_{32} + K_{12} + 3\mathcal{C})(A\partial_{\bar\eta}A - \bar{A}\partial_\eta A),\end{aligned} \quad (9)$$

where $\partial_\eta = \partial_x + i\partial_y$, $K_{12} = K_1/K_2$, and $\mathcal{C} = d/p$. The functional form of the solution of the inhomogeneous problem is $(W_1^{[3]}, W_2^{[3]}) = (\mathcal{G}_1(z)u|A|^2 + \mathcal{G}_2(z)v|A|^2, -\mathcal{G}_2(z)u|A|^2 + \mathcal{G}_1(z)v|A|^2)$. The functions $\mathcal{G}_1$ and $\mathcal{G}_2$ depend on the elastic constants and in the confinement ratio.

Near the recovery of the twisted structure, $\mathcal{C} \simeq K_{32}/2$, the type of the bifurcation is imposed by the sign of $b \simeq 3 + K_{12} - 3K_{32}$. This elastic dependence on the winding/unwinding transition in chiral nematic liquid crystals is well known (1, 6, 8). In particular, the system undergoes a supercritical bifurcation if $b > 0$; otherwise, the winding/unwinding bifurcation is subcritical. In our case of interest, the mixture of E7 and EOS12, we have measured a first-order transition (subcritical bifurcation) between the nematic phase and the TIC phase (10). Therefore, Eq. (9) is not enough to saturate the winding/unwinding instability in our experiment. We fix this problem by considering the next nonlinear correction $\vec{W}^{[5]}$ and $|b| \ll 1$. After applying the same solvability conditions as before, we obtain

$$\begin{aligned}\frac{\gamma}{2K_2}\partial_t A = \frac{\pi^2}{d^2}(2\mathcal{C} - K_{32})A - \frac{\pi^2}{4d^2}(3 + K_{12} - 6K_{32} + 6\mathcal{C})|A|^2A + \frac{K_{12}+1}{4}\nabla^2 A + \\ \frac{1-K_{12}}{8}\partial_\eta\partial_\eta\bar{A} + \frac{\pi}{8d}(3 - 4K_{32} + K_{12} + 3\mathcal{C})(A\partial_{\bar\eta}A - \bar{A}\partial_\eta A) - \frac{5\pi^2}{16d^2}(K_{32} - \frac{7K_{12}}{40} - 1 - \frac{16\mathcal{M}}{5})|A|^4A,\end{aligned} \quad (10)$$

where $\mathcal{M}$ is the projection of the first nonlinear correction $\vec{W}^{[3]}$ into the dynamics at order $\vec{W}^{[5]}$ and is equal to

$$\begin{aligned}\mathcal{M} = -K_{32}\int_0^1 [(-\mathcal{G}_1 s_2^2 + 2\mathcal{G}_1 s^2 c_2 - s_2 c_2\partial_z\mathcal{G}_1 + s_2^2\partial_z\mathcal{G}_2)cs + (s_2^2\mathcal{G}_2 - 2c_2 s^2\mathcal{G}_2 - 2c_2 s^2\partial_z\mathcal{G}_1 + 2s_2 s^2\partial_z\mathcal{G}_2)s^2]dz' \\ + (K_{32} - K_{12})\int_0^1 [(-s_2\partial_{zz}(cs\mathcal{G}_1) + s_2\partial_{zz}(s^2\mathcal{G}_2) - 2c_2\mathcal{G}_1)\frac{cs}{2} + (-s^2\partial_{zz}(cs\mathcal{G}_1) + s^2\partial_{zz}(s^2\mathcal{G}_2) + c_2\mathcal{G}_2)s^2]dz' \\ + 4\mathcal{C}\int_0^1 [(\frac{s_2^4}{4}\partial_z\mathcal{G}_2 - s_2^2\mathcal{G}_1 + cs^3\partial_z\mathcal{G}_1 - csc_2\mathcal{G}_2 + c_2 s^2\mathcal{G}_1)cs + (cs^3\partial_z\mathcal{G}_2 - s^2 s_2\mathcal{G}_1 + s^4\partial_z\mathcal{G}_1 - 2c_2 s^2\mathcal{G}_2 + 2cs\mathcal{G}_2)s^2]dz' \\ + (1 - K_{32})\int_0^1 [(s^2\partial_z(cs\partial_z\mathcal{G}_2) - s^2\partial_z(s_2\mathcal{G}_1) + s^2\partial_z(s^2\partial_z\mathcal{G}_1) - s^2\partial_z(c_2\mathcal{G}_2) + 2\mathcal{G}_2 s_2 c_2 - \mathcal{G}_2\partial_z(s^2 c_2) + s_2^2\partial_z\mathcal{G}_2] \\ - (1 - K_{32})\int_0^1 [2s_2^2\mathcal{G}_1 + 2s^2 s_2\mathcal{G}_1 - 2c_2 s_2\mathcal{G}_2 + s_2^2\partial_z\mathcal{G}_2 - 2c_2 s^2\partial_z\mathcal{G}_2)cs + (-cs\partial_z(cs\partial_z\mathcal{G}_2) + cs\partial_z(s_2\mathcal{G}_1) - cs\partial_z(s^2\partial_z\mathcal{G}_1)] \\ + (1 - K_{32})\int_0^1 cs\partial_z(c_2\mathcal{G}_2) + 2s_2 c_2\mathcal{G}_1 - \mathcal{G}_1\partial_z(s^2 c_2) - s_2 c_2\partial_z\mathcal{G}_2 + 2c_2 s_2\mathcal{G}_1 - 2c_2 s^2\partial_z\mathcal{G}_1 + 2c_2^2\mathcal{G}_2)s^2]dz'.\end{aligned} \quad (11)$$

In the above equation, the change of variable $z' = z/d$ was employed. In the double limit $\mathcal{C} \simeq K_{32}/2$ and $b \simeq 3 + K_{12} - 3K_{32}$, the functions $\mathcal{G}_1$ and $\mathcal{G}_2$ are

$$\mathcal{G}_1(z') = -\frac{dz'}{4} + \frac{\sin(2\pi z')}{8} + \frac{\sin(4\pi z')}{48} + \frac{1}{4K_{32}}(dz' - dz'\cos(2\pi z') - \sin(2\pi z')), \quad (12)$$

$$\mathcal{G}_2(z') = \frac{z'}{4K_{32}}\sin(2\pi z') + \frac{1}{96}\cos(4\pi z'). \tag{13}$$

Thus, we obtain $\mathcal{M} = 0.11K_{12} + 0.65/K_{32} - 0.07K_{12}/K_{32} - 0.68$. Then, the sign of the quintic term in Eq. (10) is governed by $Q = K_{32} - 0.53K_{12} - 2.1/K_{32} + 0.22K_{12}/K_{32} + 1.18$, which is always positive. Finally, after rescaling time, space, and the complex parameter A, we get the dimensionless equation

$$\partial_t A = \mu A + \beta|A|^2 A - |A|^4 A + \partial_\eta\partial_{\bar\eta} A - \delta\partial_\eta\partial_\eta \bar A + \chi\left(A\partial_{\bar\eta}A - \bar A\partial_\eta A\right), \tag{14}$$

where μ is the bifurcation parameter describing the winding/unwinding transition, $\beta = -\pi^2(3 + K_{12} - 6K_{32} + 6\mathcal{C})/d^2$ controls the type of the bifurcation, $\delta = (K_{12} - 1)/2(K_{12} + 1)$, and

$$\chi = \left(\frac{16}{5Q}\right)^{1/4}\frac{3 - 4K_{32} + K_{12} + 3\mathcal{C}}{2\sqrt{2}\sqrt{1 + K_{12}}}. \tag{15}$$

controls the two-dimensional chiral effects expressed by the term $\left(A\partial_{\bar\eta}A - \bar A\partial_\eta A\right)$. This chiral term has been predicted by symmetry arguments before (7, 10). Note that the rotational transformation $A \to Ae^{i\pi/2}$ in Eq. (14) gives

$$\partial_t A = \mu A + \beta|A|^2 A - |A|^4 A + \partial_\eta\partial_{\bar\eta} A + \delta\partial_\eta\partial_\eta \bar A + i\chi\left(A\partial_{\bar\eta}A + \bar A\partial_\eta A\right). \tag{16}$$

We have termed this model the chiral-anisotropic Ginzburg-Landau (CAGL) equation in the main text. Equation (16) is variational, i.e., $\partial_t A = -\delta\mathcal{F}[A, \bar A]/\delta\bar A$, where

$$\mathcal{F} = \int\int dxdy\left[-\mu|A|^2 - \beta\frac{|A|^4}{2} + \frac{|A|^6}{3} + |\nabla A|^2 + 2\delta Re\left\{(\partial_\eta \bar A)^2\right\} - i\chi|A|^2\left(\partial_{\bar\eta}A - \partial_\eta \bar A\right)\right]. \tag{17}$$

Free energy of a very long finger. To address the stabilization of a chiral finger as an energy minimization process, we consider a finger solution $A = Re^{i\phi}$ of model Eq. (16) with longitudinal length L. The transversal profiles of the finger solution, in amplitude and phase gradient, can be approximated by $R \approx \bar R sech(x/w)$ and $\partial_x\phi \approx -\bar\Phi sech(x/w_\phi)$, respectively. We study a very long finger on a square domain, i.e., $w/L \ll 1$ and $w_\phi/L \ll 1$. Replacing the ansatz for the finger into the free energy Eq. (17), we have $\mathcal{F}[R, \phi] = L\mathcal{F}_{finger}[R, \phi]$, where

$$\begin{aligned}
\mathcal{F}_{finger}[R,\phi] = &-\mu\bar R^2\int_{-L}^{L} sech^2(x/w)dx - \frac{\beta\bar R^4}{2}\int_{-L}^{L} sech^4(x/w)dx \\
&+ \frac{\bar R^6}{3}\int_{-L}^{L} sech^6(x/w)dx + \frac{(1+\delta)\bar R^2}{w^2}\int_{-L}^{L} sech^2(x/w)\tanh^2(x/w)dx + (1+\delta)\bar\phi^2\bar R^2\int_{-L}^{L} sech^2(x/w)sech^2(x/w_\phi)dx \\
&+ \frac{2\chi\bar R^3}{w}\int_{-L}^{L} sech^3(x/w)\tanh(x/w)\sin(2w_\phi\bar\phi\tan^{-1}[\tanh(x/2w_\phi)])dx \\
&- 2\chi\bar R^3\bar\phi\int_{-L}^{L} sech^3(x/w)sech(x/w_\phi)\cos(2w_\phi\bar\phi\tan^{-1}[\tanh(x/2w_\phi)])dx \\
&\equiv F_o w + \frac{2(1+\delta)}{3w}\bar R^2 + (1+\delta)\bar R^2\bar\Phi^2 I_5(w, w_\phi) + 2\chi\bar R^3 I_6(w, w_\phi, \bar\Phi) - 2\chi\bar R^3\bar\Phi I_7(w, w_\phi, \bar\Phi).
\end{aligned} \tag{18}$$

In the above equation, we have used the limit $L/w \gg 1$ to calculate the first four integrals, and we defined $F_o = -2\mu\bar R^2 - 2\beta\bar R^4/3 + 16\bar R^6/45$. A numerical exploration of the five energy terms in Eq. (18) show that $F_o w \approx (1+\delta)\bar R^2\bar\Phi^2 I_5(w, w_\phi)$ when $\delta \to 0$, and that $2(1+\delta)\bar R^2/w$ is negligible. Therefore, the transversal energy of the finger can be simplified to $\mathcal{F}_{finger}[R, \phi] \approx 2F_o w + 2\chi\bar R^3 I_6(w, w_\phi, \bar\Phi)/w - 2\chi\bar R^3\bar\Phi I_7(w, w_\phi, \bar\Phi)$. We minimize $\mathcal{F}_{finger}[R, \phi]$ with respect to w, considering the limit $w_\phi/w \ll 1$, and obtain at leading order $w^3 \approx 3\pi^3\chi w_\phi^3\bar R^3\bar\Phi/4F_o$. Note that $\partial I_6/\partial w = 0$ due to the odd symmetry of the integrand.

Local speed-curvature equation. To shed light on the interface dynamics of the cholesteric phase, at the rounded tips of CF1 or at the interface of chiral bubbles, we perform a nonlinear analysis around the interface of the chiral bubble solution, that is $A_{cb} = R_o e^{i\phi}$ in Eq. (16). Note that here we do not take into account the phase jump in ϕ (10), as we are interested in the branching dynamics away from the center of the chiral bubble. Changing variables in Eq. (16), $A = Re^{i\phi}$, and supposing that the temporal evolution of the phase is negligible compared to the dynamics of the modulus, which is reasonable at the interface, and that the phase only has a local linear dependence at the interface, the dynamics of the modulus R may be written in curvilinear coordinates $\{n, s\}$ and in the limit $\delta \to 0$ as

$$-v_n \partial_n R = \mu R + \beta R^3 - R^5 + \partial_{nn} R + \kappa \partial n R - \kappa^2 R + \chi \kappa R^2 + \partial_{ss} R, \tag{19}$$

where κ is the curvature, s is the arclength, and $v_n = \partial_t \mathbf{r} \cdot \hat{\mathbf{n}}$ is the speed normal to the interface (described by a position vector $\mathbf{r}$). Equation (19) is the evolution of the modulus $R = |A|$ in the sharp-interface limit $\kappa \ll \sqrt{3/4}$ (11). We have used the local approximation $\partial_s \phi \approx \kappa$ for the phase.

Near the Maxwell point μ_{MP}, the modulus of the interface of the chiral bubble can be approximated by the flat front solution $R_o = [3/4(1 + e^{\sqrt{3/4}n})]^{1/2}$ (10, 12). Now, we introduce curvature and chirality to the flat front by performing a weakly nonlinear analysis near the critical point $\{\mu_{MP}, \chi_o\}$. We introduce the ansatz $R(n, s, t) = R_o(n) + \epsilon^{1/2} R_1 + \epsilon R_2 + \epsilon^{3/2} R_3$, $\mu = \mu_{MP} + \epsilon^{3/2}\mu_1$, $\chi = \chi_o + \epsilon^{1/2}\chi_1$, $v_n = \epsilon^{3/2} v_N$, $\partial_s = \epsilon^{1/2}\partial_S$ and $\kappa = \epsilon^{1/2}\tilde{\kappa}$ with $\epsilon \ll 1$ into Eq. (19), and solve at every order in ϵ by applying solvability conditions (as we have elaborated already in this Supporting Information text). At order $\epsilon^{3/2}$, we obtain the speed-curvature (or Gibbs-Thomson (13)) relation

$$v_N = -|\mu_1| A + B\chi_1 \tilde{\kappa} + C\tilde{\kappa}^3 + D\partial_{SS}\tilde{\kappa}, \tag{20}$$

where

$$A = \frac{\langle |\partial_n R_o| | R_o \rangle}{\langle \partial_n R_o | \partial_n R_o \rangle} > 0, \tag{21}$$

$$B = \frac{\langle |\partial_n R_o| | R_o^2 \rangle}{\langle \partial_n R_o | \partial_n R_o \rangle} > 0, \tag{22}$$

$$D = \frac{\langle |\partial_n R_o| | f(n) \rangle}{\langle \partial_n R_o | \partial_n R_o \rangle} > 0, \tag{23}$$

and

$$C = \frac{\langle \partial_n R_o | \{-6R_o f(n) g(n) - f(n)^3 + 20 R_o^3 f(n) g(n) + 10 R_o^2 f(n)^3 - \partial_n g(n) + f(n) - \chi_o (f(n)^2 + R_o g(n))\} \rangle}{\langle \partial_n R_o | \partial_n R_o \rangle} > 0. \tag{24}$$

In the above equations, we have used the inner product $\langle q_1 | q_2 \rangle = \int_{-\infty}^{\infty} q_1 q_2 dn$. $f(n)$ and $g(n)$ are functions associated to the corrections of the modulus R. The functional form of $f(n)$ and $g(n)$ can be obtained numerically and with it approximate the coefficients C and D.

The interfacial equation (20) can be transformed into the reference-frame independent equations of motion (14)

$$\dot{\tilde{\kappa}} = -(\partial_{SS} + \tilde{\kappa}^2) U, \tag{25}$$

$$\dot{g} = 2g\tilde{\kappa} U, \tag{26}$$

where g is the curve metric, and $U = -|\mu_1| A + B\chi_1 \tilde{\kappa} + C\tilde{\kappa}^3 + D\partial_{SS}\tilde{\kappa}$. Considering the arclength $S = \int_0^{\sigma} \sqrt{g(\sigma')} d\sigma'$, where σ is the variable parameterizing the interface, and introducing the full form of U in Eqs. (25) and (26), we get

$$\dot{\tilde{\kappa}} = |\mu_1| A \tilde{\kappa}^2 - B\chi_1 \tilde{\kappa}^3 - C\tilde{\kappa}^5 - B\chi_1 \partial_{SS}\tilde{\kappa} - D\partial_{SSSS}\tilde{\kappa} - C\tilde{\kappa}(\partial_S \tilde{\kappa})^2 - (3C + D)\tilde{\kappa}^2 \partial_{SS}\tilde{\kappa}, \tag{27}$$

$$\dot{S} = \int_0^{S'} (-|\mu_1| A\tilde{\kappa} + B\chi_1 \tilde{\kappa}^2 + C\tilde{\kappa}^4 + D\tilde{\kappa}\partial_{SS}\tilde{\kappa}) dS'. \tag{28}$$

As the growth of the cholesteric interface must be variational, that is, introducing the good twist in the frustrated sample to minimize the energy in the system, the restriction D=3C is needed. Indeed, both constants have the same sign. From Eqs. (27) and (28), one can see that at a linear stage, a modulational instability with wavelength $2\pi\sqrt{D}/\sqrt{B\chi_1}$ can destabilize a flat front ($\tilde{\kappa} = 0$). The subsequent nonlinear dynamics at the cholesteric interface shape the morphologies of the rounded tips.

Repulsion between two very long fingers. In numerical integrations of Eq. (16), we have seen that repulsion between two infinite fingers (at $x = \pm x_o(t)$) is mediated by a non-trivial phase structure between them. Then, we decided to approximate this interaction by taking into account only the effect at zeroth order of the phase structure near $x = 0$ in one finger (at $x = x_o(t)$). In terms of the complex field we have $A = R(t)e^{i\phi(t)}$, where $R(t) = R(x - x_o(t))$ and $\partial_x\phi(t) = \partial_x\phi(x - x_o(t)) + \theta_b(x)$. The variable $\theta_b(x)$ represents the phase gradient shape near $x = 0$. Numerical observations show that the tail of θ_b behaves as $C_o e^{-bx}/x$, where C_o and b are positive constants. We approximate the transversal profiles of the finger by bell-shaped soliton functions, $R \approx \bar{R} sech(x/w)$ and $\partial_x\phi \approx -\bar{\Phi} sech(x/w_\phi)$. We rely on the variational form of our model to extract the key features of the interaction (15). The chiral-anisotropic Ginzburg-Landau Equation is variational, $\partial_t A = -\delta\mathcal{F}/\delta A^*$, that is

$$\partial_t \mathcal{F} = -\int |\partial_t A|^2 dxdy. \tag{29}$$

Introducing the moving frame of reference $A(x - x_o)$, and considering the limit $x_o >> \{w, w_\phi\}$, into Eq. (17) we obtain the temporal variation of the energy

$$\begin{aligned}\partial_t \mathcal{F} = -L\dot{x}_o \int_0^\infty dx \Big\{ &-2\mu R(\partial_z R) - 2R^3(\partial_z R) + 2R^5(\partial_z R) + 2(\partial_x R)(\partial_{zx} R) + 2R(\partial_z R)(\partial_x\phi)^2 + 2R^2(\partial_x\phi)(\partial_{xz}\phi) \\ &+ 2R(\partial_z R)\theta_b^2 + 4R(\partial_z R)(\partial_x\phi)\theta_b + 2R^2(\partial_{zx}\phi)\theta_b + 6\chi R^2(\partial_z R)(\partial_x\phi) + 2\chi R^3(\partial_{xz}\phi) + 6\chi R^2(\partial_z R)\theta_b \Big\},\end{aligned} \tag{30}$$

where $z = x - x_o$ and L is the longitudinal length of the finger. Changing the integration variable from x to z, Eq. (30) reduces to

$$\partial_t \mathcal{F} = -L\dot{x}_o \int_{-x_o}^\infty dz \left\{ 2R(\partial_z R)\theta_b(z + x_o)^2 + 4R(\partial_z R)(\partial_z\phi)\theta_b(z + x_o) + 2R^2(\partial_{zz}\phi)\theta_b(z + x_o) + 6\chi R^2(\partial_z R)\theta_b(z + x_o) \right\}. \tag{31}$$

Now, we take the limit $x_o \to \infty$ and introduce the tail behavior of θ_b, that is $C_o \exp(-bx)/x$. The first term in the integral of Eq. (31) can be neglected, as we retain only to first order in $\exp(-bx_o)/x_o$. Then, we have to analyze three terms

$$T_1 = 4C_o \frac{\bar{R}^2\bar{\Phi}}{w} \frac{e^{-bx_o}}{x_o} \int_{-\infty}^\infty sech^2\left(\frac{z}{w}\right) tanh\left(\frac{z}{w}\right) sech\left(\frac{z}{w_\phi}\right) e^{-bz} dz, \tag{32}$$

$$T_2 = 2C_o \frac{\bar{R}^2\bar{\Phi}}{w_\phi} \frac{e^{-bx_o}}{x_o} \int_{-\infty}^\infty sech^2\left(\frac{z}{w}\right) tanh\left(\frac{z}{w_\phi}\right) sech\left(\frac{z}{w_\phi}\right) e^{-bz} dz, \tag{33}$$

$$T_3 = -6\chi C_o \frac{\bar{R}^3}{w} \frac{e^{-ax_o}}{x_o} \int_{-\infty}^\infty sech^3\left(\frac{z}{w}\right) tanh\left(\frac{z}{w}\right) e^{-bz} dz, \tag{34}$$

where we have introduced the functional form proposed for the transversal profiles of the cholesteric finger. All the integrals listed above are negative. This is because the exponential term makes smaller the positive side of the hyperbolic tangent function. Hereafter, we name the absolute value of the integrals I_1, I_2, and I_3. Replacing all into Equation (29) we obtain at dominant order

$$\dot{x}_o = \frac{\left(-4\frac{\bar{\Phi}}{w} I_1 - 2\frac{\bar{\Phi}}{w_\phi} I_2 + 6\chi\bar{R}\frac{I_3}{w}\right)}{\left(\frac{2}{3w} + 2\bar{\Phi}^2 \int_{-\infty}^\infty sech^2\left(\frac{z}{w}\right) sech^2\left(\frac{z}{w_\phi}\right) dz\right)} C_o \frac{e^{-bx_o}}{x_o} = \mathcal{N}(\chi,\mu)\frac{e^{-bx_o}}{x_o}. \tag{35}$$

We find numerically that the constant $\mathcal{N}(\chi,\mu)$ is positive in a range of χ values at fixed $\mu = -0.4$ (Fig. S3). Therefore, the interaction between cholesteric fingers is repulsive at zeroth order. We can integrate Eq. (35) to obtain the temporal dependence of x_o

$$x_o = \frac{W((C_1 + \mathcal{N}(\chi,\mu)t)/e) + 1}{a}, \tag{36}$$

where C_1 is a constant, which depends on the initial conditions, e is the Euler number and W is the Lambert function.

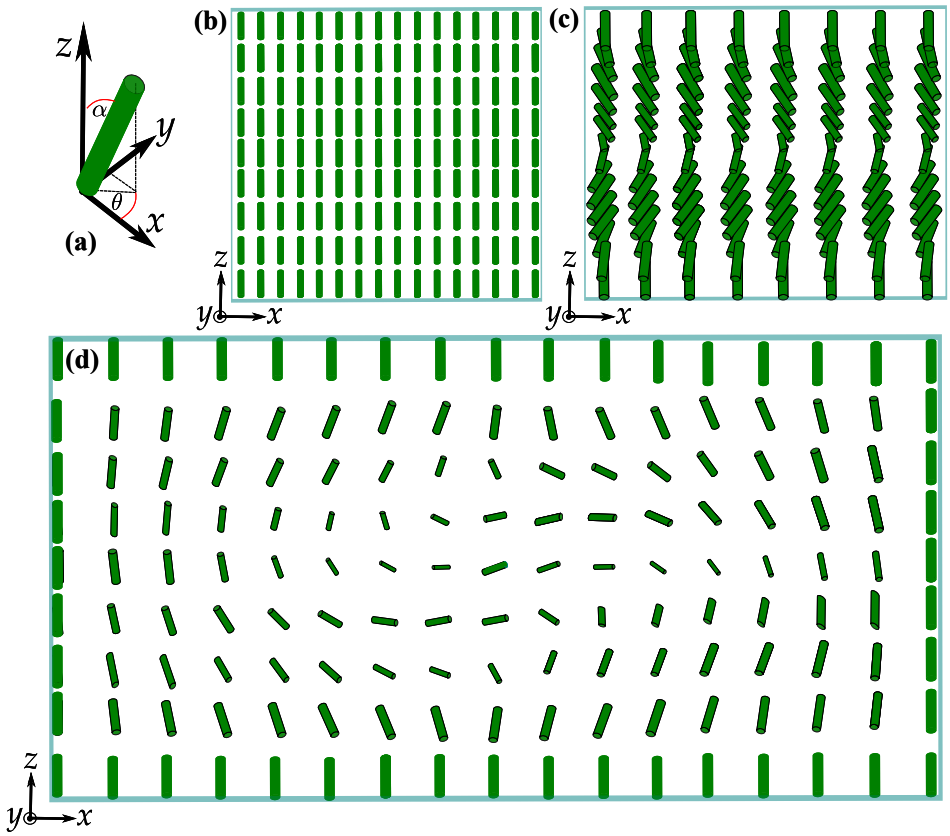

Fig. S1. Schematic representation of nematic director within a cell of thickness d with homeotropic boundary conditions. **a** Representation of the nematic director $\vec{n}$ as tubes in a spherical coordinate system. The angle α represents the tilt of $\vec{n}$ from the z-axis and θ corresponds to the angle between the x-axis and the projection of $\vec{n}$ in the plane $x-y$. **b** Nematic phase induced by homeotropic anchoring. **c** Translationally invariant configuration (TIC) is characterized by a uniform twist parallel to the cell thickness. **d** Director distribution of the cross-section of a cholesteric finger of type I far from its tips. In this case, spatial modulations of $\vec{n}$ are in z and in the plane $x-y$. This director representation is adapted from (16).

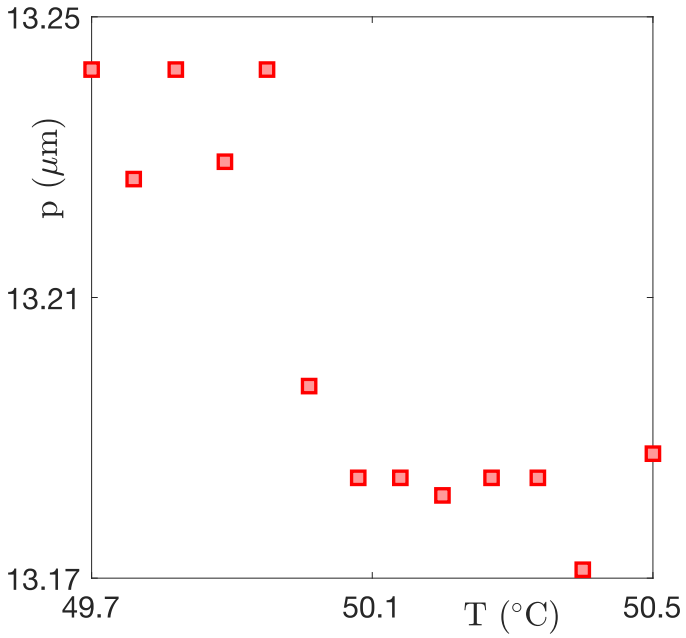

Fig. S2. Temperature dependence of the cholesteric pitch p of the mixture between E7 and EOS-12 at 7 wt% within the range 49.7°C-50.5°C.

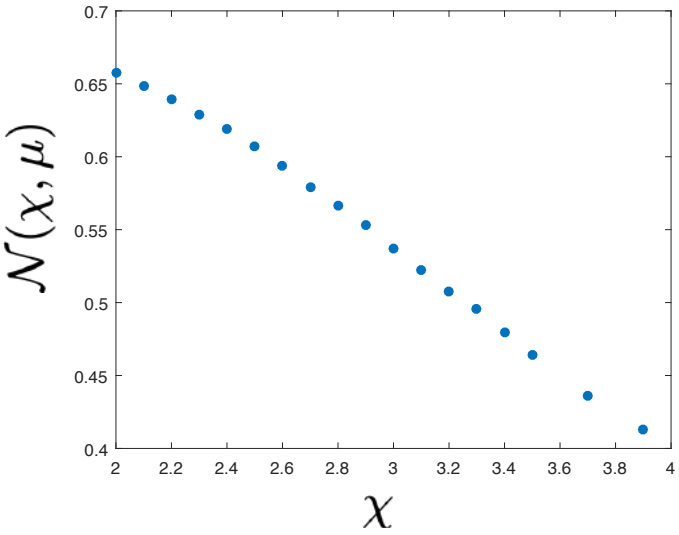

Fig. S3. Numerical values of the constant $\mathcal{N}(\chi,\mu)$ with μ=-0.4, b =0.31.

Movie S1. This movie shows an example of branching dynamics in chiral nematic liquid crystals under crossed polarizers. It corresponds to cell #1 (T =51.3°C, p=3.4 μm, d/p <58.8). The nucleation sites are chiral bubbles created by cooling closed loops of CF1.

References

1. P Oswald, P Pieranski, *Nematic and Cholesteric Liquid Crystals.* (CRC Press, London), (2005).
2. PG de Gennes, J Prost, *The Physics of Liquid Crystals.* (Clarendon Press, Oxford, UK), 2 edition, (1993).
3. AB Harris, RD Kamien, TC Lubensky, Molecular chirality and chiral parameters. *Rev. Mod. Phys.* **71**, 1745 (1999).
4. S Chandrasekhar, *Liquid Crystals.* (Cambridge University Press, Cambridge, UK), (1992).
5. T Frisch, S Rica, P Coullet, JM Gilli, Spiral waves in liquid crystal. *Phys. Rev. Lett.* **72**, 1471 (1994).
6. P Ribiere, S Pirkl, P Oswald, Electric-field-induced phase transitions in frustrated cholesteric liquid crystals of negative dielectric anisotropy. *Phys. Rev. A* **44**, 8198 (1991).
7. T Frisch, L Gil, JM Gilli, Two-dimensional landau-de gennes dynamical model for the unwinding transition of a cholesteric liquid crystal. *Phys. Rev. E* **48**, R4199 (1993).
8. P Oswald, J Baudry, S Pirkl, Static and dynamic properties of cholesteric fingers in electric field. *Phys. Reports* **337**, 67 (2000).
9. F Lequeux, P Oswald, J Bechhoefer, Influence of anisotropic elasticity on pattern formation in a cholesteric liquid crystal contained between two plates. *Phys. Rev. A* **40**, 3974 (1989).
10. MG Clerc, G González-Cortés, S Echeverría-Alar, Localized dissipative vortices in chiral nematic liquid crystal cells. *Phys. Rev. Res.* **4**, L022021 (2022).
11. A Karma, WJ Rappel, Phase-field method for computationally efficient modeling of solidification with arbitrary interface kinetics. *Phys. Rev. E* **53**, R3017 (1996).
12. MG Clerc, C Falcón, Localized patterns and holesolutions one-dimensional extended systems. *Phys. A* **356**, 48 (2005).
13. LM Pismen, *Patterns and interfaces in dissipative dynamics.* (Springer Science & Business Media), (2006).
14. RC Brower, DA Kessler, J Koplik, H Levine, Geometrical models of interface evolution. *Phys. Rev. A* **29**, 1335 (1984).
15. MC Cross, PC Hohenberg, Pattern formation outside of equilibrium. *Rev. Mod. Phys.* **65**, 851 (1993).
16. M Press, A Arrott, Static strain waves in cholesteric liquid crystals.-i. homeotropic boundary conditions. *J. de Physique* **37**, 387–395 (1976).